Scaling of plate tectonic convection with pseudoplastic rheology

Jun Korenaga[1]

Received 26 April 2010; revised 19 July 2010; accepted 1 September 2010; published 12 November 2010.

[1] The scaling of plate tectonic convection is investigated by simulating thermal convection with pseudoplastic rheology and strongly temperature-dependent viscosity. The effect of mantle melting is also explored with additional depth-dependent viscosity. Heat flow scaling can be constructed with only two parameters, the internal Rayleigh number and the lithospheric viscosity contrast, the latter of which is determined entirely by rheological properties. The critical viscosity contrast for the transition between plate tectonic and stagnant lid convection is found to be proportional to the square root of the internal Rayleigh number. The relation between mantle temperature and surface heat flux on Earth is discussed on the basis of these scaling laws, and the inverse relationship between them, as previously suggested from the consideration of global energy balance, is confirmed by this fully dynamic approach. In the presence of surface water to reduce the effective friction coefficient, the operation of plate tectonics is suggested to be plausible throughout the Earth history.

Citation: Korenaga, J. (2010), Scaling of plate tectonic convection with pseudoplastic rheology, *J. Geophys. Res.*, *115*, B11405, doi:10.1029/2010JB007670.

1. Introduction

[2] Simulating mantle convection with plate tectonics in a fully dynamic manner has become popular in the last decade or so [e.g., *Bercovici*, 2003], and quite a few studies have been published addressing a variety of problems, including the significance of 3-D spherical geometry [*Richards et al.*, 2001; *van Heck and Tackley*, 2008; *Foley and Becker*, 2009], the role of history-dependent rheology [e.g., *Tackley*, 2000; *Ogawa*, 2003; *Landuyt et al.*, 2008], the initiation of subduction [*Solomatov*, 2004; *Gurnis et al.*, 2004], and applications to other terrestrial planets [e.g., *Lenardic et al.*, 2004; *O'Neill and Lenardic*, 2007; *Landuyt and Bercovici*, 2009]. Around the same time, interests in the initiation and evolution of plate tectonics over the Earth history have grown considerably [e.g., *Mojzsis et al.*, 2001; *Bleeker*, 2003; *Harrison et al.*, 2005; *Stern*, 2005; *Korenaga*, 2006; *Van Kranendonk et al.*, 2007; *O'Neill et al.*, 2007; *Condie and Pease*, 2008; *Bradley*, 2008; *Harrison*, 2009; *Herzberg et al.*, 2010]. Many of previous numerical studies on plate tectonic convection are, however, exploratory in nature, and scaling laws relevant to such geological questions are yet to be established. Given the lack of consensus on why plate tectonics can take place on Earth to begin with [e.g., *Moresi and Solomatov*, 1998; *Gurnis et al.*, 2000; *Bercovici and Karato*, 2003; *Korenaga*, 2007], it may be premature to discuss the scaling of plate tectonic convection, but it is nonetheless important to seek a strategy to bridge geology and geodynamics by taking into account peculiar complications associated with plate tectonics.

[3] In this study, I attempt to derive the scaling of plate tectonic convection using the so-called pseudoplastic rheology [*Moresi and Solomatov*, 1998], in which the strength of plates is controlled by temperature-dependent viscosity as well as brittle failure. It is known that, for this approach to be successful, the friction coefficient for brittle deformation has to be at least 1 order of magnitude lower than suggested by laboratory experiments. The presence of pore fluid deep in the oceanic lithosphere is required to explain such low friction, and because oceanic lithosphere is likely to be very dry upon its formation by melting under mid-ocean ridges [*Hirth and Kohlstedt*, 1996; *Evans et al.*, 2005], it may appear to be difficult to justify the pseudoplastic approach. The upper half of oceanic lithosphere, however, can be pervasively fractured by thermal cracking, and in the presence of surface water, the deep hydration of oceanic lithosphere is possible [*Korenaga*, 2007]. In this mechanism, the strong temperature dependency of mantle rheology actually enhances thermal cracking. Another concern with the pseudoplastic rheology is that it is determined only by the instantaneous stress state and does not have any memory to simulate preexisting weakness, though this limitation is not as grave as it may appear. With the thermal cracking hypothesis, the stiffest part of oceanic lithosphere is continually damaged as it ages, so preexisting weakness is globally distributed. Also, whatever the actual weakening mechanism would be, oceanic lithosphere is eventually subducted (on the timescale of 100 Myr), and its memory of weakness would keep being lost in the deep mantle. For the evolution of oceanic lithosphere, therefore, the difference between instantaneous rheology and history-

[1]Department of Geology and Geophysics, Yale University, New Haven, Connecticut, USA.

0148-0227/10/2010JB007670

dependent rheology is not expected to be vital [*Tackley*, 2000]. In plate tectonics, convective heat loss is dominated by that from oceanic plates, so even with simple pseudoplastic rheology, we may still hope to capture the gross characteristics of mantle convection relevant to the long-term evolution of Earth.

[4] The purpose of this paper is two-fold. First, I will investigate the scaling of plate tectonic convection with "standard" pseudoplastic rheology, which is controlled by friction-based yield stress and temperature-dependent viscosity. Though there exist a number of numerical studies using this rheology, the temperature dependency of mantle viscosity is fairly weak in most of these studies [e.g., *Moresi and Solomatov*, 1998; *Lenardic et al.*, 2004; *Stein et al.*, 2004; *O'Neill and Lenardic*, 2007]; the maximum viscosity variation due to temperature dependency is usually 10^6. This may not seem to be low because it is high enough to put convection in the stagnant lid regime without pseudoplastic rheology. In basally heated convection, which is commonly adopted by those previous studies, there is an important difference regarding thermal structure between stagnant lid convection and plate tectonic convection. In the stagnant lid regime, most of temperature variations are taken up by the top thermal boundary layer, so viscosity variation across the top boundary layer is close to the maximum viscosity variation employed. In the plate tectonic regime with basal heating, the top and bottom thermal boundary layers have similar temperature contrasts; that is, the temperature contrast across the top boundary layer (or plates) is basically halved, with the corresponding viscosity variation of only 10^3. As explained in more detail later (section 2.1), the viscosity contrast across oceanic lithosphere due to temperature dependency is expected to be at least $\exp(20) \sim 5 \times 10^8$. It is important to use strongly temperature-dependent viscosity so that we can discuss the scaling of plate tectonic convection with more confidence. The second objective of this paper is to discuss the effects of mantle melting by adding depth-dependent viscosity to the standard pseudoplastic rheology. How mantle melting could modify the scaling of plate tectonics has important implications for the thermal evolution of Earth [*Korenaga*, 2003, 2006], but this issue has not been quantified by fully dynamic calculations.

[5] This paper is organized as follows. After describing the details of theoretical formulation (section 2), I will present numerical results, together with scaling analysis to understand the systematics of model behavior (section 3). In the discussion (section 4), I will briefly explore how new scaling laws may be used to infer when plate tectonics initiated on Earth and how it evolved subsequently. Critiques on previous attempts to derive the scaling of plate tectonics are also provided.

2. Theoretical Formulation

2.1. Mantle Rheology

[6] For temperature-dependent viscosity, I employ the following linear exponential form:

$$\eta_T^* = \exp[\theta(1 - T^*)], \tag{1}$$

where viscosity is normalized by reference viscosity η_0 defined at $T^* = 1$. Temperature is normalized as

$$T^* = \frac{T - T_s}{\Delta T}, \tag{2}$$

where T_s is the surface temperature (~273 K), and ΔT is the (arbitrary) temperature scale. The degree of temperature dependency is controlled by the Frank-Kamenetskii parameter θ, which can be related to the activation energy E as [e.g., *Solomatov and Moresi*, 2000]

$$\theta = \frac{E\Delta T}{R(T_s + \Delta T)^2}, \tag{3}$$

where R is the universal gas constant. For E of ~300 kJ mol^{-1} [e.g., *Karato and Wu*, 1993] and ΔT of ~1300 K, for example, θ is ~20.

[7] The coldest part of the lithosphere would be very stiff due to this strongly temperature-dependent viscosity, but it can also deform by brittle failure. In the continuum limit, this brittle behavior can be modeled by nonlinear effective viscosity that is adjusted to ensure the stresses remain bounded by the yield stress envelope [*Moresi and Solomatov*, 1998]. The yield stress criterion for brittle deformation may be expressed as

$$\tau_y = c_0 + \mu\rho_0 g z, \tag{4}$$

where c_0 is the cohesive strength, μ is the friction coefficient, ρ_0 is reference density, g is gravitational acceleration, and z is depth. Using the length scale D, which is the depth of a fluid layer, and the stress scale $\eta_0\kappa/D^2$, where κ is thermal diffusivity, the criterion may be nondimensionalized as

$$\tau_y^* = \tau_0^* + \tau_1^* z^*, \tag{5}$$

where

$$\tau_0^* = \frac{c_0 D^2}{\kappa\eta_0}, \tag{6}$$

and

$$\tau_1^* = \frac{\mu\rho_0 g D^3}{\kappa\eta_0}. \tag{7}$$

Using the Rayleigh number defined as

$$Ra = \frac{\alpha\rho_0 g\Delta T D^3}{\kappa\eta_0}, \tag{8}$$

where α is thermal expansivity, the criterion can also be expressed as

$$\tau_y^* = \tau_0^* + \gamma Ra\, z^*, \tag{9}$$

where

$$\gamma = \frac{\mu}{\alpha\Delta T}. \tag{10}$$

In this study, the cohesive strength is assumed to be negligibly small compared to the depth-dependent component,

and τ_0^* is set to $\tau_1^* \times 10^{-5}$. This is a reasonable approximation given experimental data on rock friction at low hydrostatic pressure [e.g., *Byerlee*, 1978] and also allows me to focus on the single parameter γ. Note that a nonzero cohesive strength term appearing for experimental data at high confining pressures could arise from a pressure-dependent friction coefficient with zero cohesive strength.

[8] The nonlinear effective viscosity for the plastic deformation is calculated as

$$\eta_y^* = \frac{\tau_y^*}{e_{\mathrm{II}}^*}, \tag{11}$$

where e_{II}^* is the second invariant of the (nondimensionalized) strain rate tensor. The transition between plastic and ductile deformation is handled by using the harmonic mean of the temperature-dependent viscosity and the above effective viscosity as

$$\eta^* = \left(\frac{1}{\eta_T^*} + \frac{1}{\eta_y^*}\right)^{-1}. \tag{12}$$

The effective viscosity for plastic deformation η_y^* is calculated for any deformation, but when stresses are smaller than the yield stress (i.e., η_y^* is large), the harmonic mean above will be dominated by η_T^*.

[9] The linear exponential form of temperature-dependent viscosity (equation (1)) predicts much smaller viscosity variation across the entire lithosphere than the more realistic Arrhenius form, $\exp(E/RT)$, but because the above pseudo-plastic rheology effectively eliminates a drastic viscosity increase in the upper half of the lithosphere, the difference between the linear exponential and Arrhenius forms is actually small [*Solomatov*, 2004]. It is still important to use the realistic value of θ as it controls the strength of the lower half of the lithosphere.

[10] When considering the effects of mantle melting, I will add depth-dependent viscosity as

$$\eta^* = \left(\frac{1}{\eta_T^* Z(z^*)} + \frac{1}{\eta_y^*}\right)^{-1}, \tag{13}$$

where

$$Z(z^*) = \begin{cases} \Delta\eta & \text{for } z^* \le h^* \\ 1 & \text{for } z^* > h^*, \end{cases} \tag{14}$$

where h^* is the thickness of dehydrated mantle and $\Delta\eta$ is a viscosity contrast introduced by dehydration.

2.2. Governing Equations and Heating Mode

[11] The nondimensionalized governing equations for thermal convection of an incompressible fluid consist of the conservation of mass,

$$\nabla \cdot \mathbf{u}^* = 0, \tag{15}$$

the conservation of momentum,

$$-\nabla P^* + \nabla \cdot \left[\eta^*\left(\nabla \mathbf{u}^* + \nabla \mathbf{u}^{*T}\right)\right] - RaT^* \mathbf{e}_z = 0, \tag{16}$$

and the conservation of energy,

$$\frac{\partial T^*}{\partial t^*} + \mathbf{u}^* \cdot \nabla T^* = \nabla^2 T^* + H^*. \tag{17}$$

The unit vector pointing downward is denoted by $\mathbf{e}_z$. The spatial coordinates are normalized by the length scale D, and time is normalized by the diffusion timescale, D^2/κ. Velocity $\mathbf{u}^*$ is thus normalized by κ/D. Dynamic pressure P^* and heat generation H^* are normalized by $\eta_0\kappa/D^2$ and $k\Delta T/(\rho_0 D^2)$, respectively, where k is thermal conductivity.

[12] In this study, I will focus on thermal convection that is purely internally heated, by using the insulated bottom boundary condition. There will be no thermal boundary layer at the bottom, simplifying the scaling analysis of numerical results. This heating mode is also appropriate for the majority of the Earth history [*Korenaga*, 2008a, section 5.1]. At the same time, a temperature contrast across the fluid layer is not known *a priori*, so the maximum temperature, $T_{\max}^*$, is not guaranteed to be unity. Some *a posteriori* rescaling is thus necessary. The Frank-Kamenetskii parameter is recalculated from its original value θ_0 as

$$\theta = \theta_0 T_{\max}^*, \tag{18}$$

so that $\exp(\theta)$ corresponds to the actual maximum viscosity variation due to temperature dependency. The internal Rayleigh number may also be defined with $T_{\max}^*$ as

$$Ra_i = Ra\ T_{\max}^* \exp[\theta_0(T_{\max}^* - 1)], \tag{19}$$

in which the total temperature contrast is $T_{\max}^* \Delta T$, and the internal viscosity, η_i, is assumed to be $\eta_0 \exp[\theta_0(1 - T_{\max}^*)]$. Because of purely internal heating, the surface heat flux q is, at a statistical equilibrium, equal to total heat generation in the fluid divided by surface area

$$q = \rho_0 DH, \tag{20}$$

and the corresponding Nusselt number is calculated as

$$Nu = \frac{q}{kT_{\max}^* \Delta T/D} = \frac{H^*}{T_{\max}^*}. \tag{21}$$

[13] The internal heating ratio (IHR), ξ, is the difference between heat flux out of the top boundary and that into the bottom boundary, normalized by the former [e.g., *McKenzie et al.*, 1974], i.e.,

$$\xi = \frac{Nu_{\mathrm{top}} - Nu_{\mathrm{bot}}}{Nu_{\mathrm{top}}}, \tag{22}$$

and because the bottom boundary is insulated in this study ($Nu_{\mathrm{bot}} = 0$), IHR is unity for all runs as long as H^* is positive. The internal heat production H^* does not directly correspond to the amount of radiogenic heat production in the mantle, which may be referred here as H_{rad}^*. Over the Earth history, the mantle has been (usually) cooling with time [*Abbott et al.*, 1994; *Herzberg et al.*, 2010], and in the study of mantle convection, this secular cooling is often included as part of "internal" heating. So H^* represents both radiogenic heat production and secular cooling. Secular cooling is a transient phenomenon, and directly simulating it requires us

to assume an initial condition for subsolidus mantle convection on Earth, which is hardly known. Numerical models for mantle convection are therefore typically run for a number of convective overturns to reach a statistical equilibrium so that model results do not strongly depend on employed initial conditions. This steady state modeling approach has to include secular cooling as part of internal heating, in order to simulate an Earth-like IHR. The thermal evolution of Earth can be studied reasonably well by assuming that the mantle is in a quasi steady state at each time step [e.g., *Daly*, 1980].

[14] It is important to distinguish IHR from the convective Urey ratio, *Ur*, which is the ratio of radiogenic heat production in the mantle over the mantle heat flux [*Christensen*, 1985], i.e.,

$$Ur = \frac{H^*_{\mathrm{rad}}}{Nu_{\mathrm{top}}}. \tag{23}$$

The Urey ratio is directly related to the chemical composition of Earth's mantle, and it is a key parameter to describe the thermal budget of Earth. When *Ur* is discussed, radiogenic heat production and secular cooling are considered separately. As noted by *Korenaga* [2008a], there has been some misunderstanding in the literature by confusing *Ur* with IHR or by underestimating the significance of secular cooling, and unfortunately, such confusion still seems to continue [e.g., *Deschamps et al.*, 2010]. IHR can be related to the convective Urey ratio as [*Korenaga*, 2008a]

$$\xi \approx 1 - \frac{C_c}{C_m + C_c}(1 - Ur), \tag{24}$$

where C_m and C_c are the heat capacities of the mantle and the core, respectively. The present-day Urey ratio is probably ~0.2 [*Korenaga*, 2008a], but because the core heat capacity is only ~1/5 of the whole Earth value, the present-day IHR for Earth's mantle is estimated to be ~0.9 [*Korenaga*, 2008a]. Based on thermal history considerations, the Urey ratio may have been higher in the past [*Korenaga*, 2006; *Herzberg et al.*, 2010], so IHR is likely to have been closer to unity than at present. To first order, therefore, the use of purely internal heating ($\xi = 1$) appears to be a reasonable simplification.

2.3. Notes on Modeling Strategy

[15] Besides the use of pseudoplastic rheology, the numerical model of mantle convection as specified previously is kept simple to facilitate the interpretation of modeling results, and the potential significance of realistic complications, which are neglected in this study, are discussed in the following.

[16] Because of the insulating boundary condition, bottom heat flux is zero, so there are no upwelling plumes in the model. The influence of plumes on plate dynamics thus cannot be examined. Because of the nearly unity IHR expected for Earth's mantle (section 2.2), however, such influence may not be of first order. The governing equations employed are based on the Boussinesq approximation [e.g., *Schubert et al.*, 2001], so adiabatic gradients are zero (i.e., the total temperature contrast $T^*_{\mathrm{max}}\Delta T$ is the superadiabatic temperature contrast), and the model temperature corresponds to potential temperature. The effects of compressibility on the gross characteristics of thermal convection have been known to be rather minor [*Jarvis and McKenzie*, 1980; *Bercovici et al.*, 1992].

[17] For the ductile deformation of the mantle, the Newtonian rheology with linear exponential temperature dependency is adopted (equation (1)), but mantle rheology is known to be much more complex depending on, at least, stress, pressure, grain size, and chemical composition [e.g., *Karato and Wu*, 1993]. In case of pseudoplastic rheology, the difference between the Arrhenius rheology and its linear exponential approximation is not important as already mentioned, and I choose to use the latter because it is specified by only one nondimensional parameter θ, whereas the Arrhenius-type temperature dependency requires three [e.g., *Korenaga*, 2009]. Non-Newtonian, stress-dependent rheology can be approximated by Newtonian rheology if the activation energy is properly scaled [*Christensen*, 1984]. The importance of pressure dependence caused by the activation volume is not clear at the moment. First of all, activation volumes for mantle rheology are still poorly known even for upper mantle minerals [*Korenaga and Karato*, 2008]. Second, viscosity increase with increasing pressure should be at least partly cancelled by viscosity decrease with increasing temperature along the mantle adiabat. With the Boussinesq approximation employed here, the use of pressure-independent rheology actually requires nonzero activation volume, the effect of which is assumed to be cancelled exactly by temperature variations along the adiabat. Grain size variation can affect mantle dynamics considerably [e.g., *Solomatov*, 1996], but how grain size should evolve in the convecting mantle is still poorly understood, so it appears premature to consider its effect in this study. The effect of composition on mantle rheology is taken into account when dehydration stiffening is effected by depth-dependent viscosity (equation (14)). There are of course other compositional effects [e.g., *Karato*, 2008], but the effect of dehydration appears to be most important at least for the upper mantle rheology [e.g., *Karato et al.*, 1986; *Mei and Kohlstedt*, 2000a, 2000b; *Faul and Jackson*, 2007], and mantle dehydration is always expected whenever mantle melts [*Hirth and Kohlstedt*, 1996].

[18] Another important rheological aspect for large-scale mantle dynamics is a viscosity jump at the base of the upper mantle, which has been estimated to be on the order of ~10–100 primarily through the geodynamical modeling of Earth's geoid [e.g., *Hager*, 1984]. Such inference is, however, also known to suffer from considerable nonuniqueness [e.g., *King*, 1995; *Kido and Cadek*, 1997], and the viscosities of the upper and lower mantle may not be very different if the mantle transition zone has a lower viscosity [*Soldati et al.*, 2009]. Furthermore, even if the lower mantle does have a higher viscosity than the upper mantle, it applies only for the present-day situation. When the mantle was hotter in the past, the viscosity contrast may be smaller or even reversed if the lower mantle rheology is more temperature dependent (i.e., higher activation energy) than the upper mantle counterpart. Rheological stratification in the mantle is an important subject, but these uncertainties imply a variety of situations to be considered, so it is left for future studies.

[19] The mantle transition zone is also characterized by multiple phase transitions, and in particular, the effects of the

endothermic phase change at the base of the transition zone on large-scale mantle circulation was once a popular topic in geodynamics [e.g., *Christensen and Yuen*, 1984; *Tackley et al.*, 1993; *Solheim and Peltier*, 1994; *Yuen et al.*, 1994]. Numerical studies with strong plates exhibit, however, only a modest influence of endothermic phase change on mantle dynamics [e.g., *Zhong and Gurnis*, 1994], and recent experimental studies further suggest that the Clapeyron slope of the endothermic phase change is likely to be only -1.3 MPa K^{-1} [*Katsura et al.*, 2003; *Fei et al.*, 2004], which is much less negative than previously thought. Modeling phase transitions, therefore, is not considered to be essential.

[20] Finally, the model is 2-D Cartesian, whereas the use of a 3-D spherical shell would be most appropriate. The restriction to 2-D modeling is primarily to generate a large number of modeling results (with modest computational resources) so that scaling analysis becomes more robust, though I do not expect scaling laws to change drastically by moving from 2-D to 3-D. The effect of sphericity would likely be of minor nature [*Bercovici et al.*, 2000]. On the basis of isoviscous convection models using 3-D spherical shells, for example, *Deschamps et al.* [2010] recently derived the following heat flow scaling (adapted here for the case of purely internal heating):

$$Nu \approx 0.59 f^{0.05} Ra^{0.300-0.003f}, \tag{25}$$

where f is the ratio of the core radius to the total radius of a planet. The ratio f is 0.55 for Earth and unity for Cartesian, so it can be seen that sphericity has virtually no impact on this scaling.

[21] The convection model of this study is, therefore, simple but probably not simpler than necessary. In any event, this study should provide a reference point, by which the effects of any additional complication can be quantified in future.

3. Numerical Results and Scaling Analysis

[22] The finite element code of *Korenaga and Jordan* [2003] was used to solve the coupled Stokes flow and thermal advection-diffusion equations (15)–(17). The benchmark tests of this code can be found in work by *Korenaga and Jordan* [2003] for Newtonian rheology and *Korenaga* [2009] for non-Newtonian rheology. To reduce wall effects, the aspect ratio of the convection model is set to 8, and the model domain is discretized with 400×50 uniform 2-D quadrilateral elements. With this mesh resolution, model parameters are chosen so that Nu does not exceed 20 and the top thermal boundary layer contains at least a few elements vertically on average. The nondimensional surface temperature is fixed to zero, and the bottom boundary is insulated. The top and bottom boundaries are free slip, and a reflecting boundary condition is applied to the side boundaries. In all cases, Ra is set to 10^6, but Ra_i varies greatly because of different combinations of θ_0 and H^* (and thus $T^*_{\max}$).

[23] The initial temperature condition is specified as

$$T^*(x^*, z^*) = z^* + a\cos(\pi x^*)\sin(\pi z^*) + \epsilon, \tag{26}$$

where a is usually 0.2, and ϵ is random fluctuation with the amplitude of 10^{-3}. When the assumed mantle rheology is appropriate for the operation of plate tectonic convection, this initial condition quickly brings the system to that mode of convection. Otherwise, the system gradually migrates into the mode of stagnant lid convection. If I start with a uniformly hot fluid instead, the system always begins with stagnant lid convection, and sublithospheric mantle is heated up considerably until the onset of plate tectonics. Very low viscosity (and thus very high convective velocity) beneath the stagnant lid during this initial period means exceedingly small time steps for numerical integration, so this type of initial condition is not computationally efficient when aiming at statistically steady states required for scaling analysis.

3.1. Convection Diagnostics

[24] A typical snapshot of model run is shown in Figure 1a. This is the case of $\gamma = 0.6$, $\theta_0 = 15$, and $H^* = 20$, with the standard pseudoplastic rheology (equation (12)). In addition to $T^*_{\max}$, I calculate two more measures for the temperature scale. One is the domain average temperature,

$$\langle T^* \rangle = \iint T^* dx^* dz^* \Big/ \iint dx^* dz^*, \tag{27}$$

and the other is the (self-consistent) internal temperature [*Korenaga*, 2009],

$$T_i^* = \frac{1}{1-\delta'} \int_{\delta'}^{1} \left(\int T^* dx^* \Big/ \int dx^* \right) dz^*, \tag{28}$$

where $\delta' = T_i^*/H^*$.

[25] The vigor of convection can be quantified by calculating the root-mean-square velocity v^*_{rms}, and a velocity diagnostic most indicative of the mode of convection is the root-mean-square surface velocity v^*_s. To quantify how plate-like the surface velocity field is, *Weinstein and Olson* [1992] introduced the notion of "plateness," and for convection exhibiting multiple plates with different velocities, I use the definition of plateness

$$P_x = \int_{e' < x} dx^* \Big/ \int dx^*, \tag{29}$$

where

$$e' = \frac{1}{v_s^*} \left| \frac{dv^*(z^* = 0)}{dx^*} \right|. \tag{30}$$

The parameter P_x measures the fraction of surface with normalized strain rate e' smaller than the given threshold x. The velocity profile shown in Figure 1b, for example, has $P_{0.1}$ of 0.76 (Figure 1c). Like other definitions of plateness, P_x varies from 0 to 1, with higher values corresponding to more rigid behavior. For comparison, actual plates on Earth tend to have wide diffuse boundary zones, which occupy ~15% of the surface area at the present day [*Gordon and Stein*, 1992].

[26] To understand the spatial distribution of viscous dissipation, I define Φ_c as the viscous dissipation within the region above $z^* = c$,

$$\Phi_c = \int_0^c \left(\int \eta^* e_{ij}^* e_{ij}^* dx^* \right) dz^*, \tag{31}$$

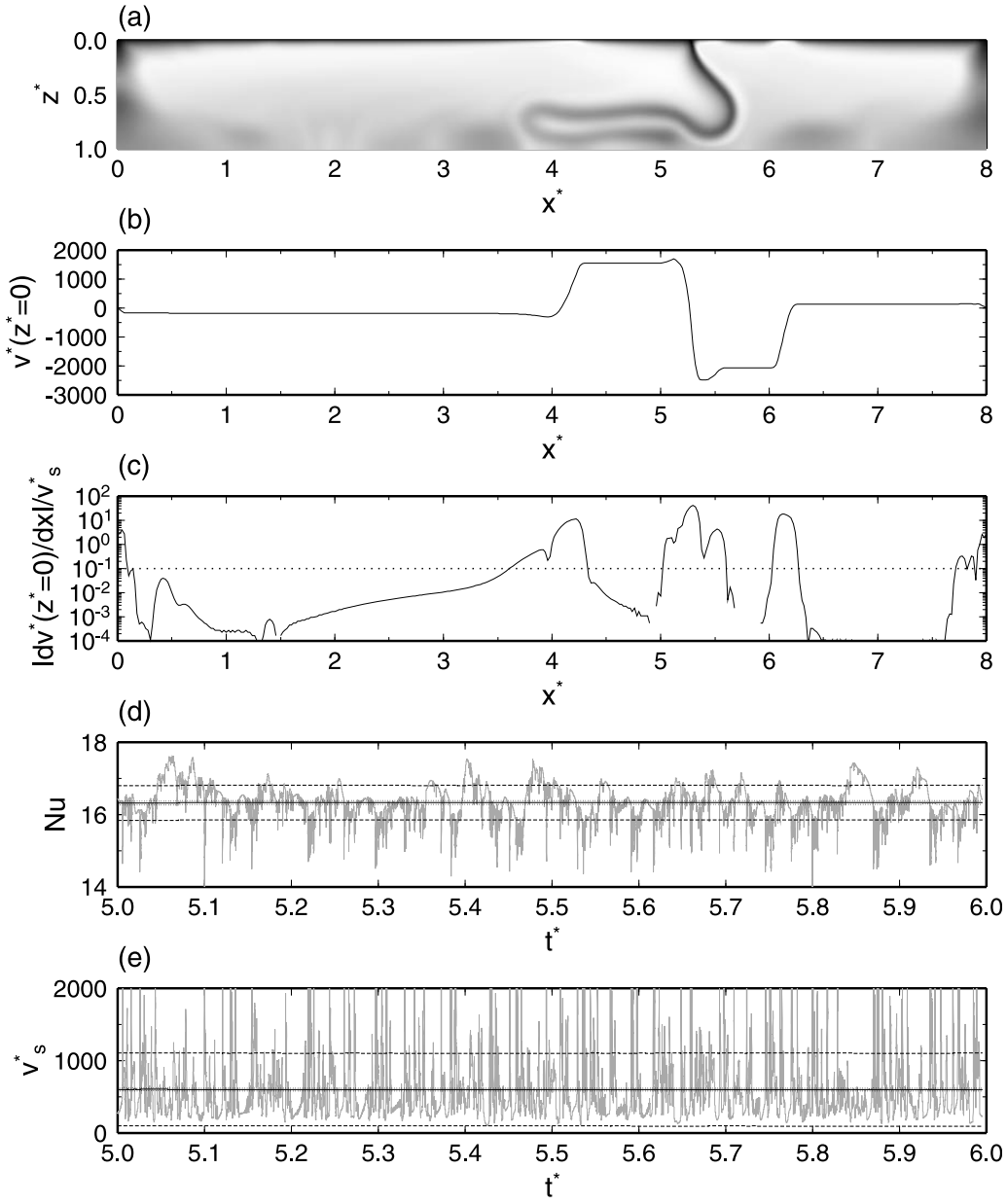

Figure 1. Example of simulation results from the case of $\gamma = 0.6$, $\theta_0 = 15$, and $H^* = 20$ with the standard pseudoplastic rheology (equation (12)). (a) Snapshot of the temperature field. Darker shading corresponds to lower temperature. (b) Surface velocity profile and (c) horizontal strain rate scaled by the average surface velocity, corresponding to the snapshot shown in Figure 1a. $P_{0.1}$ is 0.76 for this particular velocity profile; that is, 76% of the surface has the scaled strain rate lower than 0.1 (shown by a dotted line in Figure 1c). (d) Nusselt number and (e) root-mean-square surface velocity as a function of time (shown in gray). For this model run, statistically steady state was achieved at $t^* = 1.8$, and running average is taken from the subsequent model results. In Figures 1d and 1e, the running average and its uncertainty (1 σ) are shown as solid and dotted lines, respectively, and the one standard deviation of the temporal variation itself is shown by a dashed line.

and calculate Φ_δ, $\Phi_{\delta/2}$, and Φ ($\equiv\Phi_1$), where δ is (on average) the maximum thickness of the top thermal boundary layer [e.g., *Busse*, 1967],

$$\delta = 2Nu^{-1}. \tag{32}$$

Here δ is nondimensionalized by the model depth D.

[27] Each case was run up to $t^* = 6$. The cumulative heat generation and cumulative heat loss from the surface are monitored, and when these two start to match within ~1%, I judge that the system has reached statistically steady state. This usually takes place at $t^* = \sim 2$–3, and I use subsequent model results to calculate time average values of key diagnostics such as Nu and Φ. The (one) standard deviation of

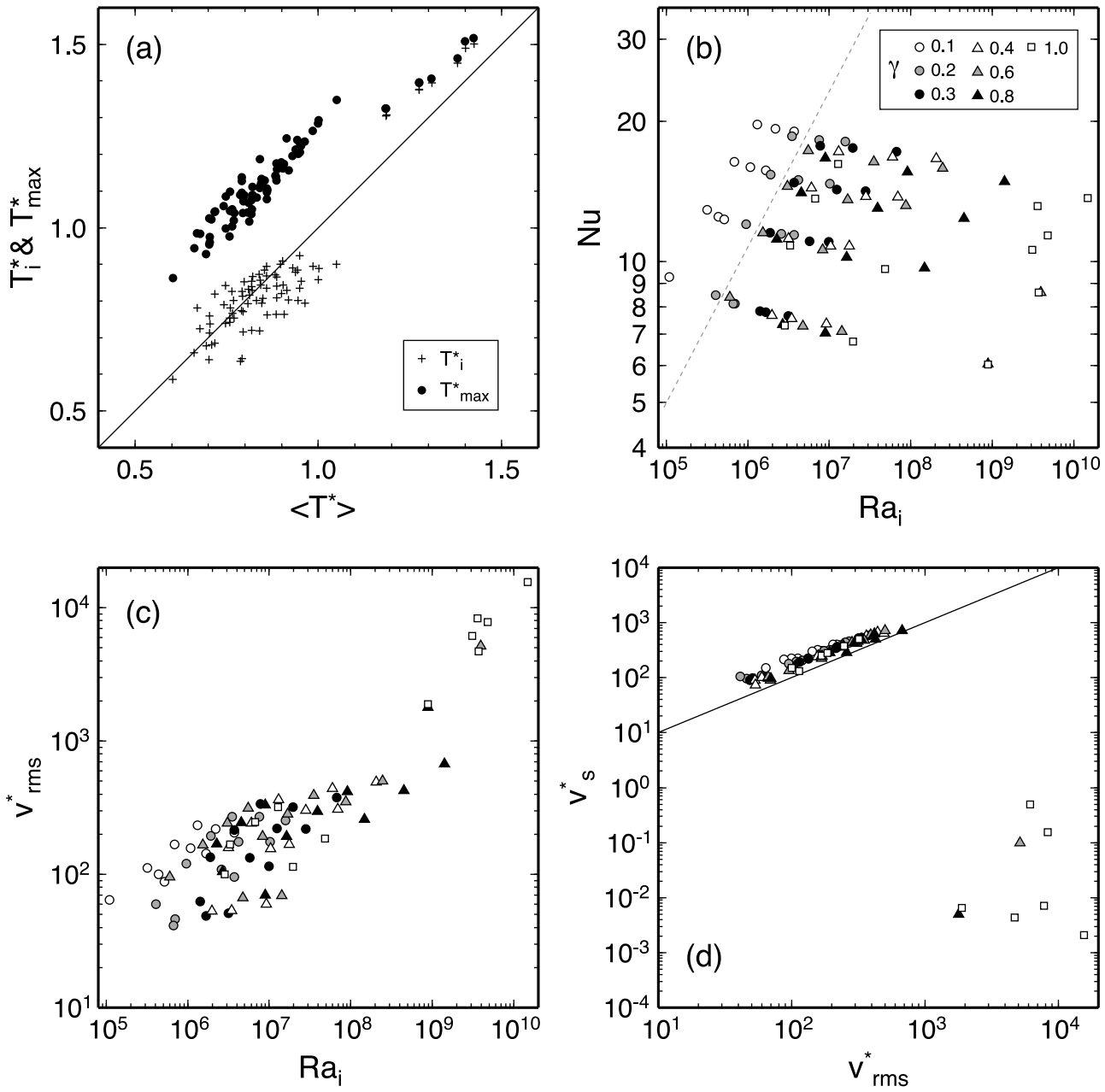

Figure 2. Correlations among convection diagnostics from reference runs: (a) internal temperature T_i* (cross) and maximum temperature T^*_{max} (solid circle) are compared with domain average temperature $\langle T^* \rangle$; (b) *Nu* and Ra_i, with a dashed line indicating the slope of $Ra_i^{1/3}$; (c) v^*_{rms} and Ra_i; and (d) v^*_s and v^*_{rms}. In Figures 2b–2d, different symbols denote runs with different γ, as shown by the legend in Figure 2b.

time-averaged *Nu* is typically less than 1%, whereas the standard deviation of *Nu* itself is often greater by 1 order of magnitude, reflecting the highly time-dependent nature of convection (Figure 1d). Surface velocity exhibits even greater time dependency (Figure 1e).

3.2. Reference Scaling

[28] A total of 82 cases were run with the standard pseudoplastic rheology using different combinations of γ (0.1–1), θ_0 (10–25), and H* (8–20). The summary of convection diagnostics is reported in Tables A1 and A2; eight runs resulted in stagnant lid convection, and others exhibited plate tectonic convection.

[29] Three different temperature scales, T^*_{max}, $\langle T^* \rangle$, and T_i*, are correlated well to each other (Figure 2a). Regardless of the mode of convection, T^*_{max} is distinctly higher than $\langle T^* \rangle$, and this is because the thickness of the top thermal boundary layer is not trivial in those runs. The maximum *Nu* achieved is only ~20 (Figure 2b), and these different temperature scales are expected to converge as *Nu* increases. Stagnant lid runs are characterized by similar T^*_{max} and T_i*, because of small temperature variations beneath the stagnant lid.

[30] The relation between Nu and Ra_i appears to roughly follow the classical scaling of $Nu \propto Ra_i^{1/3}$ within runs with the same γ and similar θ (Figure 2b). Varying γ has considerable effects on the scaling of Nu as well as $v^*_{\rm rms}$ (Figure 2c). The distinction between plate tectonic and stagnant lid runs is very clear in the correlation (or lack thereof) between $v^*_{\rm rms}$ and v^*_s (Figure 2). Average surface velocity in these plate tectonic runs is higher than corresponding $v^*_{\rm rms}$ because the latter involves averaging over the entire domain, the majority of which moves more slowly than surface plates.

[31] My scaling analysis to understand the systematics of these model results is based on the local stability of top thermal boundary layer [*Howard*, 1966]. Because of pseudoplastic rheology, the effective viscosity of the top boundary layer or the effective lithospheric viscosity, η_L, is expected to be higher than the interior viscosity, and I denote the viscosity contrast between them as

$$\Delta\eta_L = \eta_L/\eta_i. \tag{33}$$

Viscosity in the top thermal boundary layer varies considerably as specified by equation (12), and the effective lithospheric viscosity is an attempt to capture the overall stiffness of the boundary layer by just one viscosity value. For the stiff boundary layer to subduct, it has to become convectively unstable at least, and by assuming that the maximum thickness of the boundary layer δD corresponds to marginal stability, the following relation should hold:

$$\frac{\alpha\rho_0 g(T^*_{\max}\Delta T)(\delta D)^3}{\kappa\eta_L} = Ra_c, \tag{34}$$

where Ra_c is the critical Rayleigh number. By using the relation between δ and Nu (equation (32)), this marginal stability criterion may be rearranged as

$$Nu = 2\left(\frac{Ra_i}{Ra_c}\right)^{1/3}\Delta\eta_L^{-1/3} \tag{35}$$

or

$$\Delta\eta_L = \frac{8Ra_i}{Ra_c\,Nu^3}. \tag{36}$$

Hereinafter Ra_c is set to 10^3.

[32] Equation (36) may be regarded as a way to extract lithospheric viscosity contrasts from the measured pairs of Ra_i and Nu. The lithospheric viscosity contrast calculated this way increases as θ increases, and this θ sensitivity is greater for higher γ (Figure 3a). The following functionality appears to be sufficient to reproduce the first-order behavior of the viscosity contrast,

$$\Delta\eta_L(\gamma,\theta) = \exp[a(\gamma)\theta], \tag{37}$$

which converges to unity at the limit of zero θ. The coefficient $a(\gamma)$ is determined by linear regression for each group of runs with the same γ (Figure 3a). Excluding the result for γ of 0.1, the runs with which are characterized by rather low plateness (Table A1), the coefficient is linearly correlated with γ in the logarithmic space (Figure 3b), which may be expressed as

$$a(\gamma) \approx 0.327\gamma^{0.647}. \tag{38}$$

Equations (37) and (38) can predict $\Delta\eta_L$ reasonably well over the range of 4 orders of magnitude (Figure 3c). The prediction for Nu through equation (35) has the average error of ~10% (Figure 3d). This error is considerably larger than that observed for the heat flow scaling derived by *Moresi and Solomatov* [1998], which was based on convection with the aspect ratio of one. The use of the wide aspect ratio (= 8) in this study and resultant time dependency in convection patterns may be the source of these scatters.

[33] The lithospheric viscosity contrast $\Delta\eta_L$ calculated from equation (36) exhibits broad correlations with other convection diagnostics (Figure 4). Higher $\Delta\eta_L$ generally gives rise to higher plateness (Figure 4a) and greater viscous dissipation in the top boundary layer (Figure 4c). How viscous dissipation is distributed within the boundary layer, however, seems to be insensitive to variations in $\Delta\eta_L$ as $\Phi_{\delta/2}/\Phi_\delta \sim 0.5$–$0.6$ for all of plate tectonic runs (Figure 4d).

[34] Assuming the half-space cooling of lithosphere, the (average) maximum plate thickness δ is related to the average length of plates, L, as

$$\delta \sim 2\left(\frac{L}{Dv^*_s}\right)^{1/2}, \tag{39}$$

where $L/(Dv^*_s)$ is the average time from a ridge to a subduction zone. Thus, the average aspect ratio of convection cells may be calculated from Nu and v^*_s as

$$\frac{L}{D} = \frac{v^*_s}{Nu^2}, \tag{40}$$

for which equation (32) is used. The aspect ratio gradually increases as $\Delta\eta_L$ increases; that is, stronger plates tend to be longer (Figure 4b). By assuming some empirical relation for L/D (e.g., $L/D \sim \Delta\eta_L^{1/6}$), equation (40) may be rearranged as scaling for v^*_s,

$$v^*_s = 4\left(\frac{L}{D}\right)\left(\frac{Ra_i}{Ra_c}\right)^{2/3}\Delta\eta_L^{-2/3}. \tag{41}$$

That is, unlike the scaling for heat flux (equation (35)), some information on the aspect ratio of convection cells is essential for the scaling for surface velocity.

3.3. Effect of Shallow Stiffening

[35] On Earth, the creation of new plates at mid-ocean ridges is usually accompanied by the melting of upwelling mantle (unless the mantle is too cold), and this chemical differentiation along the global mid-ocean ridge system constitutes the dominant fraction of terrestrial magmatism [*Crisp*, 1984]. This mantle melting results in the formation of oceanic crust as well as depleted mantle lithosphere, both of which are chemically more buoyant with respect to the underlying asthenosphere [*Oxburgh and Parmentier*, 1977], and the depleted lithosphere also becomes intrinsically more viscous (by ~10^3) because of dehydration caused by melting [*Hirth and Kohlstedt*, 1996]. As long as plate tectonics is

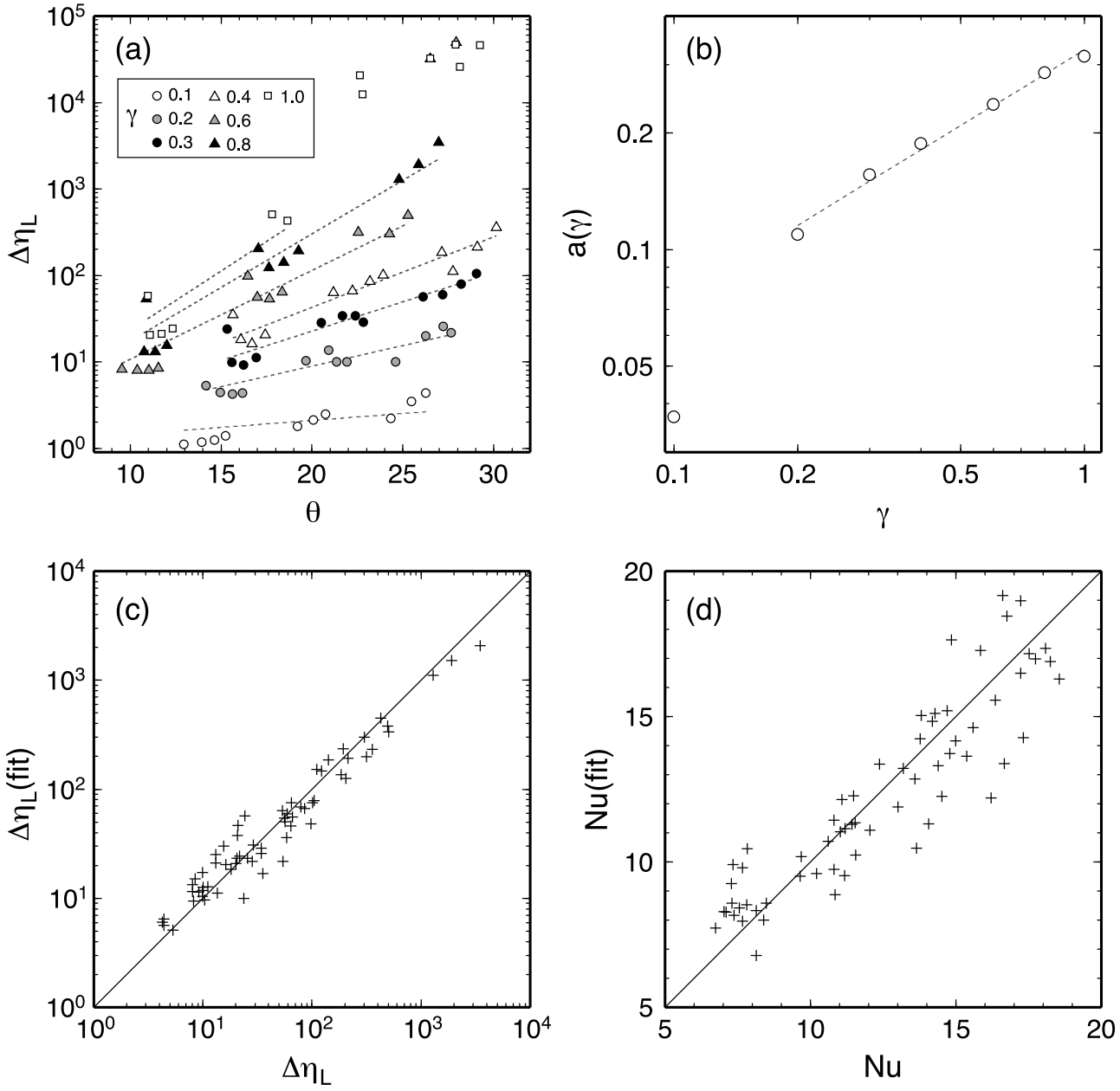

Figure 3. The systematics of reference runs can be summarized through effective lithospheric viscosity contrast $\Delta\eta_L$. (a) $\Delta\eta_L$ as a function of θ. Different symbols denote runs with different γ, and dashed lines are fitted trends in the form of equation (37) for each γ. Data with $\Delta\eta_L$ greater than 10^4 are stagnant lid runs, which are excluded from linear regression. (b) The fitted coefficient a as a function of γ. Dashed line represents equation (38). (c) Comparison of measured $\Delta\eta_L$ with predicted values based on equations (37) and (38). (d) Comparison of measured Nu with predicted values based on equation (35).

taking place, the chemical buoyancy of oceanic lithosphere is insignificant as resistance to subduction because the basalt-to-eclogite transition at relatively shallow depth (<60 km) makes the subducting slab compositionally denser than the surrounding mantle [e.g., *Ringwood and Irifune*, 1988]. In this study, therefore, I focus on the effect of dehydration stiffening on the scaling of plate tectonic convection. As in work by *Korenaga* [2009], instead of tracing the advection of the dehydrated slab through time, I use the depth-dependent viscosity that is fixed in time (equation (14)). Though the subducting slab loses the extra viscosity contrast $\Delta\eta$ as soon as it passes the given depth h^*, the effect of shallow stiffening on slab bending can still be evaluated with this scheme.

[36] The scaling of Nu equation (35) indicates that different combinations of Ra_i and $\Delta\eta_L$ can produce the same Nu. Thus, in terms of the efficiency of heat transport, a run with high Ra_i and high $\Delta\eta_L$ may be indistinguishable from that with low Ra_i and low $\Delta\eta_L$, but shallow stiffening may affect these cases differently. A wide variety of plate tectonic cases were thus simulated by varying γ (0.4–0.8), θ_0 (10–25), and H^* (2–20), and shallow stiffening was incorporated with h^* ranging from 0.1 to 0.3 and $\Delta\eta$ ranging from 3 to 10^3.

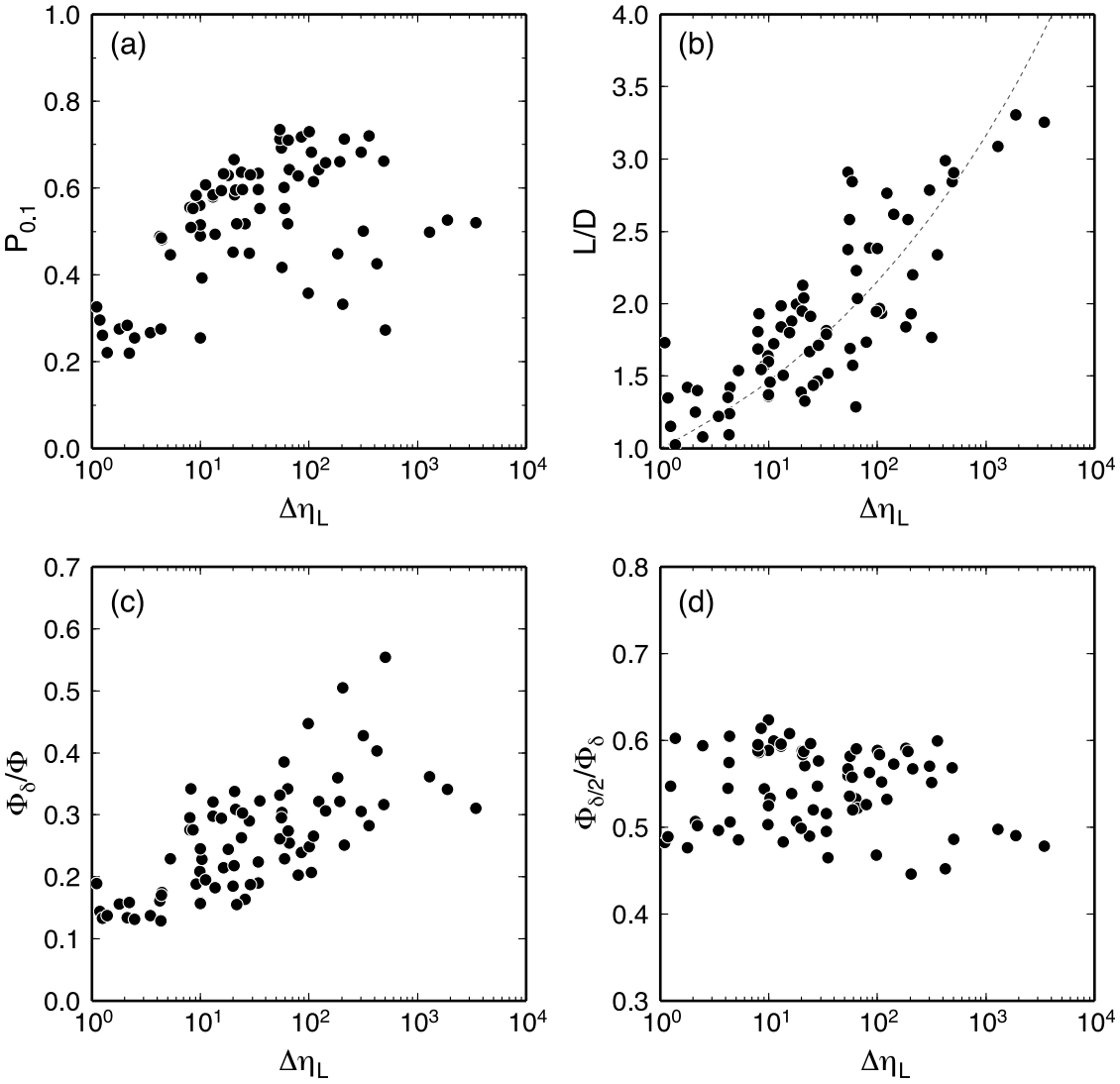

Figure 4. Covariations of measured lithospheric viscosity contrast $\Delta\eta_L$ with (a) plateness $P_{0.1}$, (b) the average aspect ratio of convection cells L/D, (c) the fraction of viscous dissipation taking place in the top thermal boundary layer with respect to that in the entire domain Φ_δ/Φ, and (d) the fraction of viscous dissipation in the upper half of the boundary layer with respect to that in the entire boundary layer $\Phi_{\delta/2}/\Phi_\delta$. Dashed line in Figure 4b corresponds to $L/D = \Delta\eta_L^{1/6}$.

Stiffening by mantle melting is limited mostly to the top 200 km or so (i.e., $h^* < 0.07$), and the use of greater h^* is to study the asymptotic behavior of stiffening effects. Also, the top thermal boundary layer in numerical modeling is thicker than actual oceanic lithosphere because of relatively low Ra_i used in this study, so h^* has to be comparably large in order to reproduce an Earth-like combination of thermal and compositional boundary layers. The number of runs is 225 in total, with 19 stagnant lid runs (Tables A3–A8). Convection diagnostics were measured in the same way for reference runs.

[37] The scaling analysis for runs with shallow stiffening is founded on that for the reference runs. As in section 3.2, the lithospheric viscosity contrast $\Delta\eta_L$ is calculated from the measured pair of Nu and Ra_i. A key issue is how this viscosity contrast is influenced by the additional depth-dependent viscosity, and this influence may be measured by the deviation from the prediction based on equation (37). The predicted viscosity contrast is based solely on γ and θ, and it is denoted as $\Delta\eta_{L,\mathrm{ref}}$ to distinguish from the actual $\Delta\eta_L$. The ratio $\Delta\eta_L/\Delta\eta_{L,\mathrm{ref}}$ is loosely correlated with $\Delta\eta$ and h^* as one may expect (Figures 5a and 5b); higher $\Delta\eta$ or h^* leads to higher $\Delta\eta_L$ than predicted by equation (37). A better correlation may be seen between the two ratios, $\Delta\eta_L/\Delta\eta_{L,\mathrm{ref}}$ and h^*/h^*_{ref} (Figure 5c), where h^*_{ref} is defined as

$$h^*_{\mathrm{ref}} = Nu^{-1}_{\mathrm{ref}}, \tag{42}$$

and

$$Nu_{\mathrm{ref}} = 2\left(\frac{Ra_i}{Ra_c}\right)^{1/3}\Delta\eta^{-1/3}_{L,\mathrm{ref}}. \tag{43}$$

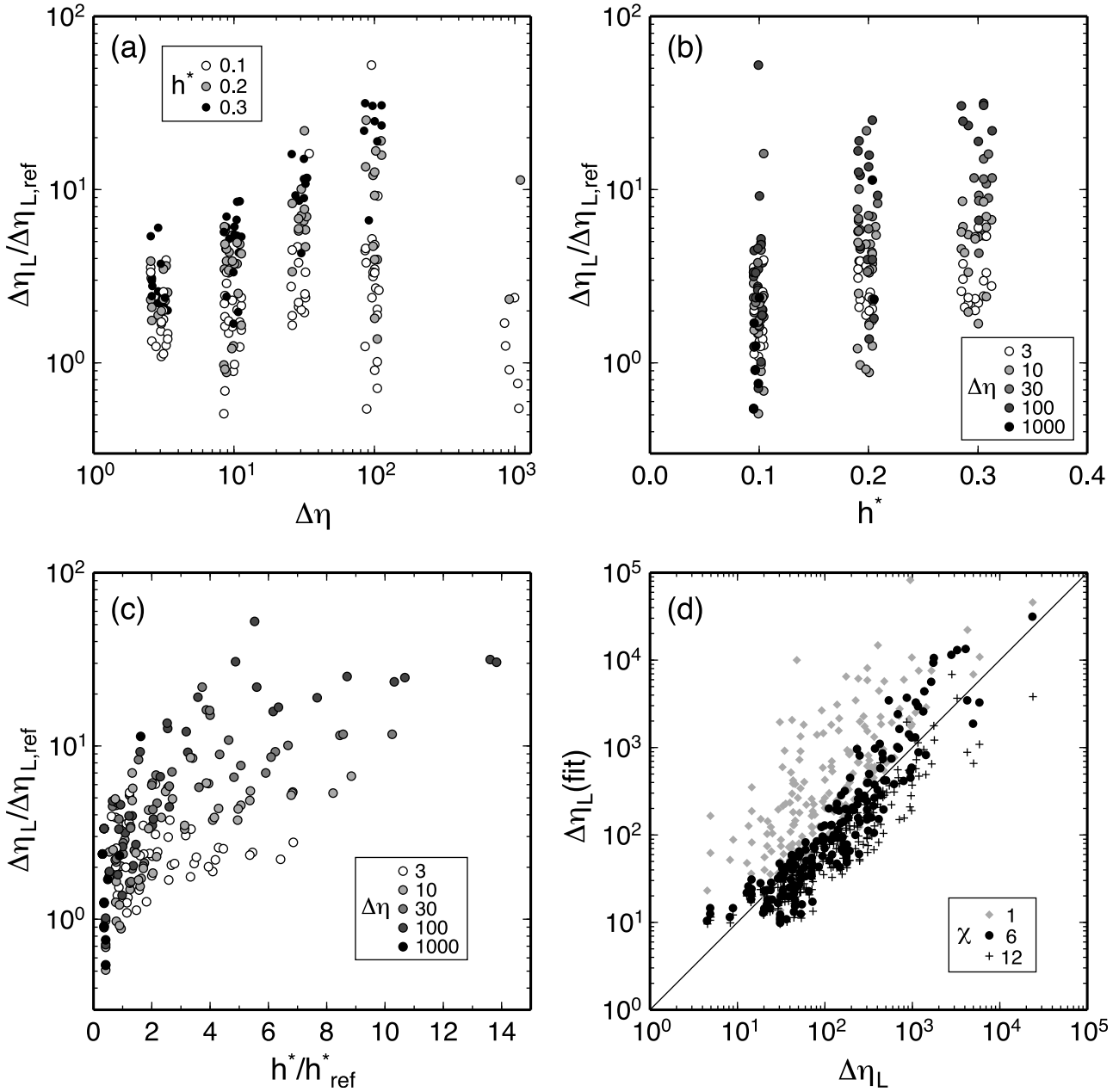

Figure 5. The effect of additional depth-dependent viscosity on the lithospheric viscosity contrast. The deviation from the prediction based on standard pseudoplastic rheology, $\Delta\eta_L/\Delta\eta_{L,\mathrm{ref}}$, is shown as a function of (a) the viscosity contrast due to dehydration $\Delta\eta$, (b) the thickness of dehydrated layer h^* , and (c) the same thickness but scaled by the reference thickness, h^*/h^*_{ref}. Different symbols denote different h^* in Figure 5a and different $\Delta\eta$ in Figures 5b and 5c. Note that in Figures 5a and 5b the values of $\Delta\eta$ and h^* are slightly perturbed randomly for display purposes. (d) Comparison of measured $\Delta\eta_L$ with predicted values based on equation (44), for three different values of χ.

The parameter h^*_{ref} is the averaged thickness of the top thermal boundary layer expected for a run with the same Ra_i but with the standard pseudoplastic rheology. The ratio $\Delta\eta_L/\Delta\eta_{L,\mathrm{ref}}$ increases as h^*/h^*_{ref} but eventually saturates and never exceeds the given $\Delta\eta$. This behavior may be represented by the functionality

$$\Delta\eta_L = \Delta\eta_{L,\mathrm{ref}} \exp\left[\ln(\Delta\eta)\max\left(1, \frac{h^*}{\chi h^*_{\mathrm{ref}}}\right)\right], \qquad (44)$$

which means that $\Delta\eta_L$ converges to the simple product of $\Delta\eta_{L,\mathrm{ref}}$ and $\Delta\eta$ when h^* is sufficiently greater than h^*_{ref}. The parameter χ controls how high h^* should be with respect to h^*_{ref} in order to achieve the convergence; greater χ means that thicker h^* is required. By trying a range of values, I found that $\chi \approx 6$ can reproduce the measured $\Delta\eta_L$ reasonably well (Figure 5d).

[38] The relations between $\Delta\eta_L$ and other convection diagnostics are more ambiguous than observed for the ref-

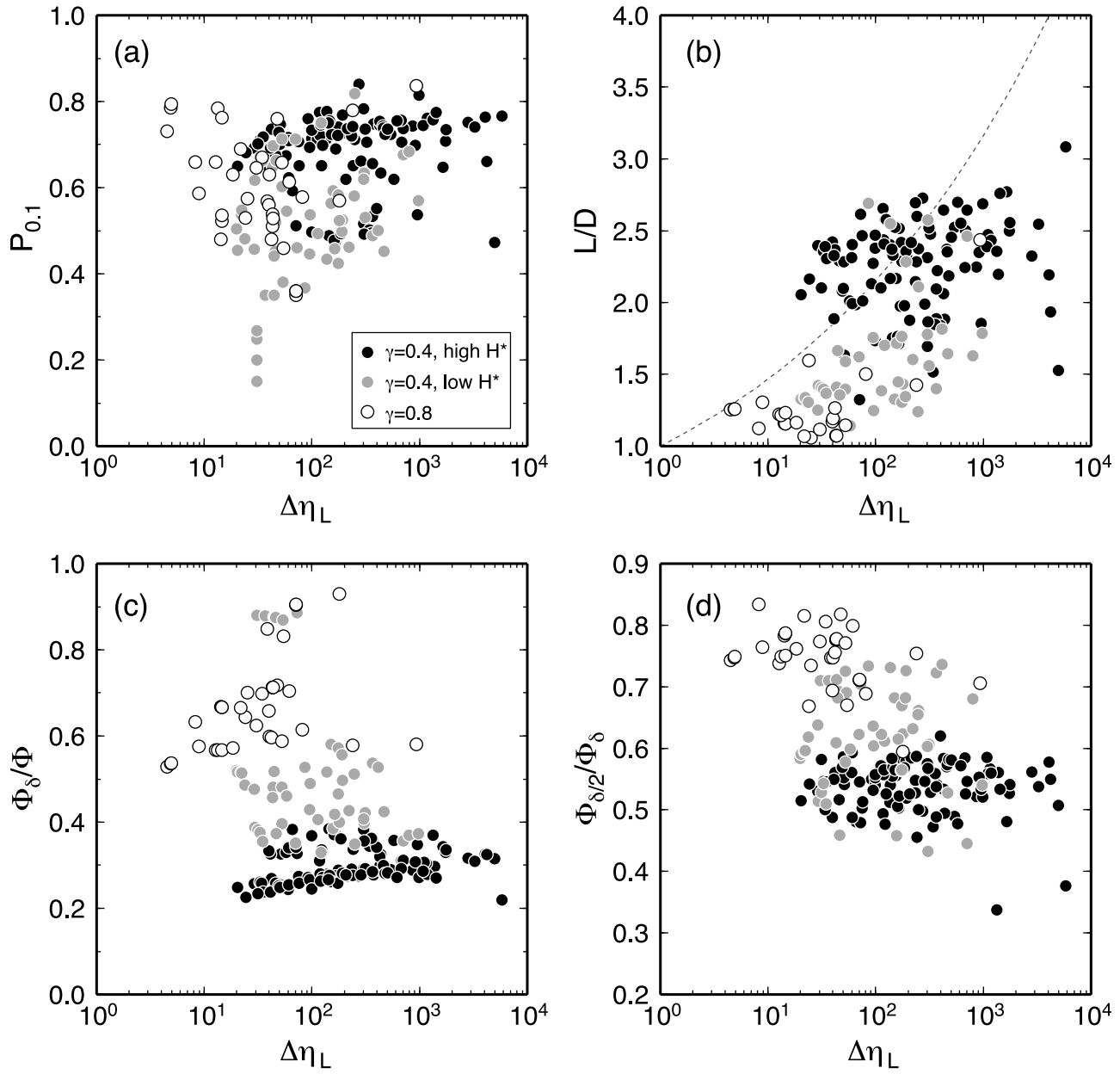

Figure 6. Same as Figure 4 but for runs with shallow stiffening. Different symbols correspond to different groups of runs: γ of 0.4 with high H^* (solid circle; Tables A3–A5), γ of 0.4 with low H^* (gray circle; Tables A6 and A7), and γ of 0.8 (open circle; Table A8).

erence runs (Figure 6). It appears to be premature to parameterize the aspect ratio L/D as a simple function of the lithospheric viscosity contrast (Figure 6b), and more thorough work is clearly required to better understand the self-organization of plate tectonics. It is still interesting to note, however, that high plateness is possible even with low viscosity contrast (Figure 6a) and that plate tectonic convection can occur even when most of viscous dissipation takes place in the top boundary layer (Figure 6c).

3.4. Conditions for Plate Tectonic Convection

[39] The condition for plate tectonic convection is found to be seen most clearly in the covariation of Ra_i and $\Delta\eta_L$ (Figure 7). Plate tectonic convection is possible even with high lithospheric viscosity contrast if Ra_i is sufficiently high, and the critical viscosity contrast, above which plate tectonic convection is unlikely, appears to be

$$\Delta\eta_{L,\mathrm{crit}} \approx 0.25 Ra_i^{1/2}, \tag{45}$$

though there are a few runs that slightly violate this threshold.

[40] To understand the meaning of this scaling, I consider stress balance at the bending of subducting slab, which is probably the most critical part of plate tectonic convection.

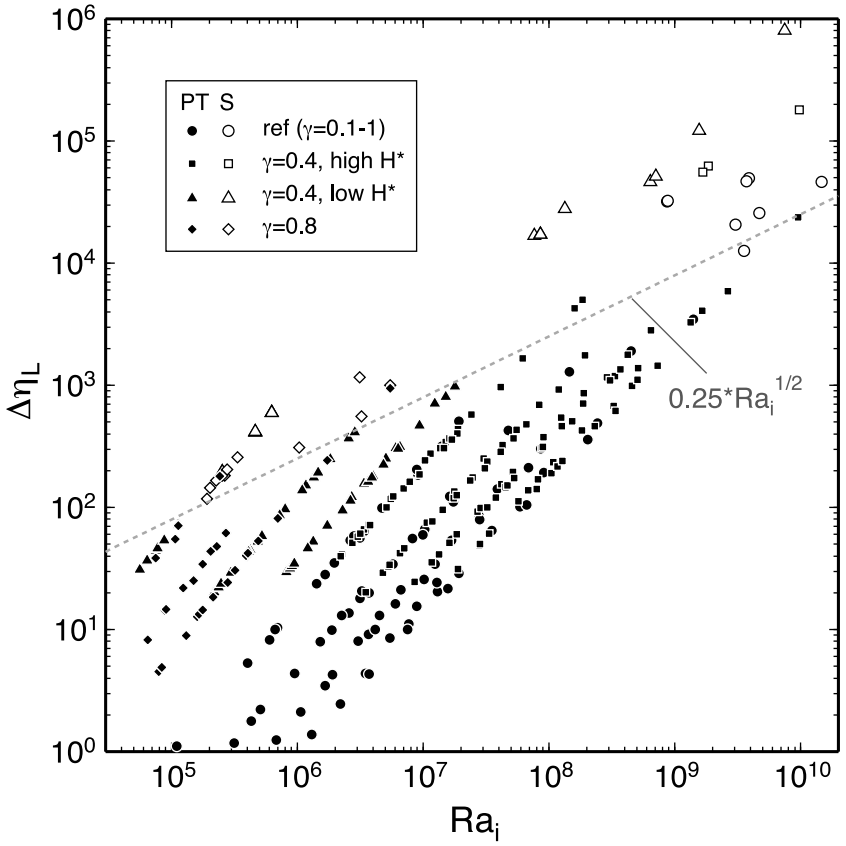

Figure 7. Covariation of Ra_i and $\Delta\eta_L$ for all model runs. Solid and open symbols denote plate tectonic and stagnant lid runs, respectively. Dashed line represents an approximate divide between these two modes of convection ($\Delta\eta_L \sim 0.25\ Ra_i^{1/2}$).

First, the stress due to the negative buoyancy of the slab may be expressed as

$$\tau_S \sim \alpha\rho_0 g(T^*_{\max}\Delta T)D, \tag{46}$$

or by normalizing the (internal) stress scale, $\eta_i\kappa/D^2$,

$$\tau_S{}^* \sim Ra_i. \tag{47}$$

Second, the bending stress should be proportional to the lithospheric viscosity and bending strain rate as [e.g., *Conrad and Hager*, 1999]

$$\tau_B \sim \eta_L \frac{v_s(\delta D)}{R^2}, \tag{48}$$

where R is the radius of curvature, and its nondimensionalized form is

$$\tau_B{}^* \sim \Delta\eta_L\, v_s^*\, \delta\left(\frac{D}{R}\right)^2 \propto \Delta\eta_L^{2/3} Ra_i^{1/3}\left(\frac{D}{R}\right)^2. \tag{49}$$

Finally, by assuming $\tau_S \approx \tau_B$ at $\Delta\eta_L = \Delta\eta_{L,\mathrm{crit}}$, we may derive the following scaling for the radius of curvature:

$$\frac{R}{D} \propto Ra_i^{-1/6}. \tag{50}$$

Thus, the radius is weakly dependent of the vigor of convection, and it becomes smaller for more vigorous convection. Without this variation in the radius of curvature, the critical viscosity contrast would be more sensitive to a change in Ra_i (i.e., proportional to Ra_i instead of $Ra_i^{1/2}$).

[41] Note that all of the 307 runs reported here are either strictly plate tectonic or stagnant lid convection, and there is no case of episodic overturn, in which the system periodically goes back and forth between plate tectonic and stagnant lid modes [*Moresi and Solomatov*, 1998]. This is consistent with the use of virtually zero cohesion strength and finite friction coefficient in this study (section 2.1), because the possibility of the episodic overturn mode appears to be important only with nontrivial cohesion strength [e.g., *Moresi and Solomatov*, 1998; *Stein et al.*, 2004; *O'Neill et al.*, 2007]. The use of purely internal heating (thus the lack of upwelling plumes) in this study might also be responsible.

4. Discussion and Conclusion

[42] On the basis of the scaling of *Nu* (equation (35)) and the parameterization of $\Delta\eta_L$ (equations (37), (38), and (44)), it is now possible to discuss the relation between mantle temperature and surface heat flux, which is fundamental to our theoretical understanding of the long-term evolution of Earth. Because some of key model parameters are still poorly

known [e.g., *Korenaga and Karato*, 2008], the following exercise should be regarded as a preliminary case study. As explained below, the self-consistent construction of a plausible heat flow scaling law requires modeling the thermal and chemical evolution of Earth at the same time, so a more extensive exploration of the scaling of plate tectonics will be reported elsewhere.

[43] First, for the dependency of viscosity on mantle potential temperature T_p, the following Arrhenius form is used:

$$\eta_T(T_p) = \eta_r \exp\left(\frac{E}{RT_p} - \frac{E}{RT_r}\right), \tag{51}$$

where η_r is reference viscosity at $T_p = T_r$, and E is assumed to be 300 kJ mol^{-1} [*Korenaga*, 2006]. The reference temperature is set to 1623 K (1350°C), which corresponds to the present-day potential temperature of the ambient mantle [*Herzberg et al.*, 2007]. The Frank-Kamenetskii parameter θ is calculated from equation (3), and the reference lithospheric viscosity contrast $\Delta\eta_{L,\mathrm{ref}}$ is calculated with γ of 0.8, which corresponds to the effective friction coefficient of ~0.02 (equation (10)).

[44] The internal Rayleigh number Ra_i is then calculated with the above temperature-dependent viscosity and the following values: $\alpha = 2 \times 10^{-5}$ K^{-1}, $\rho_0 = 4000$ kg m^{-3}, $g = 9.8$ m s^{-2}, and $D = 2900 \times 10^3$ m. The dehydration of the mantle beneath mid-ocean ridges is assumed to take place when the upwelling mantle crosses the solidus for dry pyrolitic mantle, and the initial pressure of melting (in GPa) can be calculated from the potential temperature (in K) as [*Korenaga et al.*, 2002]

$$P_o = (T_p - 1423)/100, \tag{52}$$

and the thickness of dehydrated mantle h_m is given by $P_o/(\rho_o g)$. The nondimensional thickness h^* is h_m/D, and the viscosity contrast due to dehydration $\Delta\eta$ is assumed to be 10^2 here. The lithospheric viscosity contrast $\Delta\eta_L$ gradually increases for higher T_p (Figure 8c, case 1) because hotter mantle starts to melt deeper (Figure 8b), but the effect of shallow stiffening on the viscosity contrast saturates at $T_p \sim 1600$°C, above which the contrast slightly decreases because of smaller θ for higher T_p (equation (3)).

[45] Last, the global heat flux Q is calculated as

$$Q = k A T_p Nu/D, \tag{53}$$

where A is the surface area of Earth, and k is assumed to be 4 W m^{-1} K^{-1}. The reference viscosity η_r is set to 10^{19} Pa s so that the predicted global heat flux matches the present-day convective heat flux of ~38 TW [*Korenaga*, 2008a] (Figure 8d, case 1). The effect of shallow stiffening suppresses the heat flux considerably and even reverts the sense of temperature sensitivity; the flux is lower for higher T_p above ~1450°C until the effect of shallow stiffening becomes saturated at ~1600°C. For the temperature range of 1350–1600°C, which is most relevant to the thermal evolution of Earth for the last 3.5 Gyr [*Herzberg et al.*, 2010], the predicted relation between the mantle temperature and surface heat flux closely resembles that suggested by *Korenaga* [2006] along a similar line of reasoning but on the basis of the global energy balance.

[46] Note that the reference viscosity η_r of 10^{19} Pa s (at present-day potential temperature) may be appropriate for asthenosphere but would typically be regarded as too low to represent the whole mantle, for which the viscosity of 10^{21}–10^{22} Pa s is usually assumed. The effective lithospheric viscosity contrast is ~3×10^2 in this example (Figure 8c), which is comparable to the discrepancy. Traditionally, the average viscosity of the present-day mantle is estimated to be of that magnitude, in order to explain surface heat flux (or equivalently, plate velocities) [e.g., *Hager*, 1991; *Bercovici et al.*, 2000], because the aforementioned geoid-based studies (section 2.3) can constrain only relative variations in viscosity and are insensitive to the absolute values of viscosity. The heat flow scaling of equation (35) suggests that a lithospheric viscosity contrast alone could regulate surface heat flux without invoking a viscosity increase in the lower mantle.

[47] Note that the use of constant viscosity contrast for dehydration stiffening $\Delta\eta$ for the entire temperature range (thus implicitly over the entire Earth history) is equivalent to assuming that the water content of the convecting mantle does not change with time. If the mantle is drier than present, for example, the viscosity contrast would be smaller, and if the mantle is completely dry, mantle melting should not cause any viscosity change. By combining the thermal budget of Earth with geological constraints on sea level change and with the growth of continental crust, *Korenaga* [2008b] suggested that the volume of Earth's oceans is unlikely to have been constant with time and that the mantle may have been gradually hydrated by subduction starting with a very dry state in the Archean. As the second example (denoted as case 2 in Figure 8), I consider effective heat flow scaling expected for this scenario. For simplicity, the mantle is assumed to have been hydrated linearly from the completely dry state to the present state, as it cooled from 1550°C, to 1350°C for the last ~3 Gyr [*Herzberg et al.*, 2010]. For T_p greater than 1550°C, therefore the internal viscosity is intrinsically higher by $\Delta\eta$, and this viscosity contrast gradually diminishes as T_p approaches 1350°C. This is reflected in how Ra_i varies with T_p (Figure 8a, case 2). At the same time, the viscosity contrast due to mantle melting is unity at $T_p \geq 1550$°C and gradually increases to the full value $\Delta\eta$ at T_p of 1350°C. The total lithospheric viscosity contrast $\Delta\eta_L$ in this scenario is much reduced than the previous example (Figure 8c), but because of the overall reduction in Ra_i, the surface heat flux is suppressed further, and the inverse relationship between mantle temperature and heat flux dominates heat flow scaling during the mantle hydration period (Figure 8d). Obviously, this type of calculation should be done more self-consistently by modeling the thermal evolution of Earth together with its global water cycle, and what is presented here is only a crude estimate.

[48] In both cases, the lithospheric viscosity contrast is always smaller than its threshold (Figure 8c), so plate tectonic convection seems to be dynamically plausible throughout the Earth history, as long as surface water exists to hydrate the lithosphere and reduce the effective friction coefficient [*Korenaga*, 2007]. In particular, the gradually hydrating mantle (case 2) helps to maintain relatively small

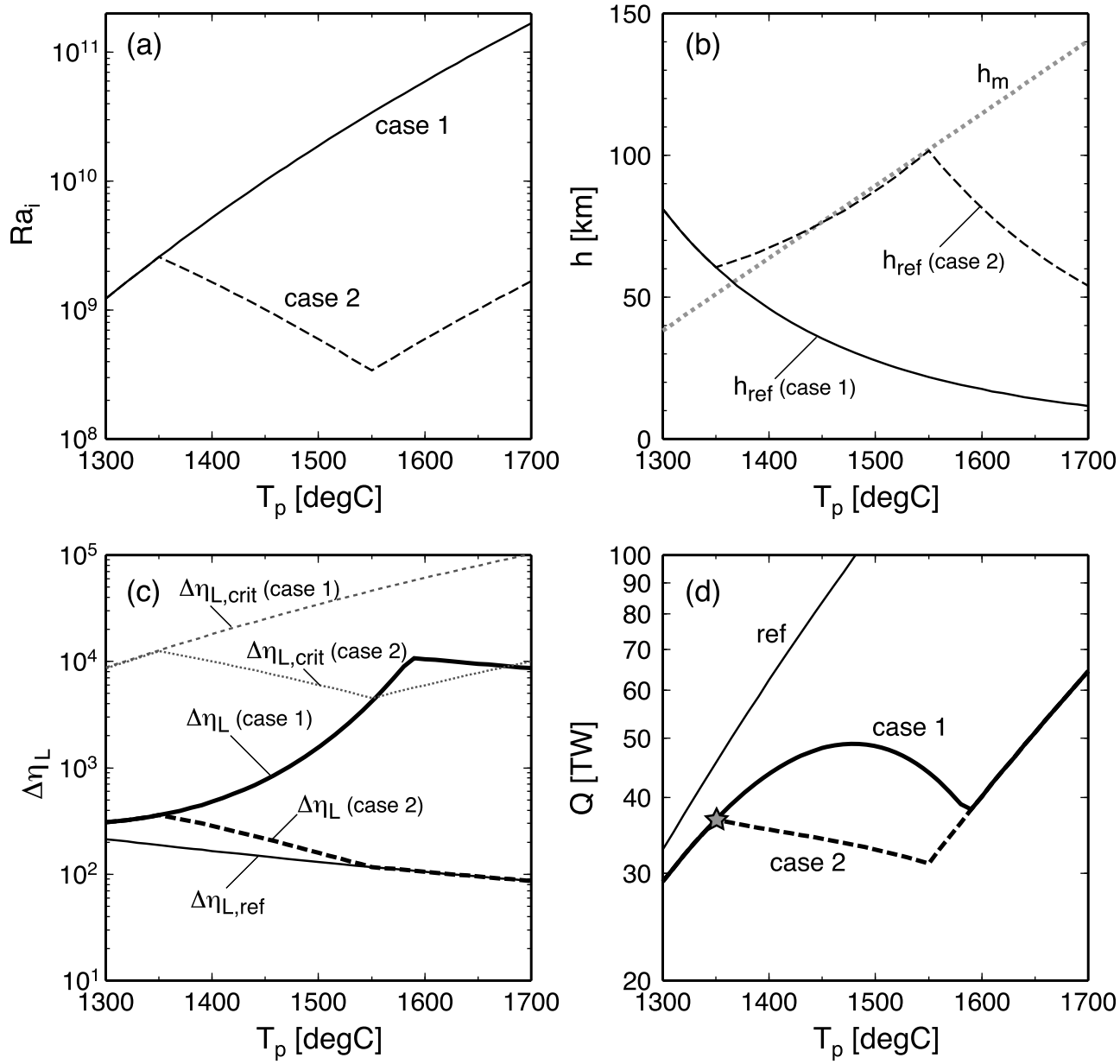

Figure 8. A worked example of how the new scaling laws of plate tectonic convection may be used to build heat flow scaling for Earth. (a) Internal Rayleigh number Ra_i as a function of mantle potential temperature T_p. (b) Thicknesses of dehydrated lithosphere (h_m, dotted line) and reference thermal boundary layer (h_{ref}, solid line for case 1 and dashed line for case 2) (equation (42)). (c) Lithospheric viscosity contrast for case 1 (thick solid line), case 2 (thick dashed line), and a reference case with no effect of mantle melting, i.e., $h_m^* = 0$ (thin solid line). Also shown are the critical viscosity contrast for plate tectonic convection (dashed line for case 1 and dotted line for case 2). (d) Relation between T_p and surface heat flux Q. Legend is the same as in Figure 8c. Star denotes convective heat flux at the present day (38 TW at 1350°C). See the main text for details.

$\Delta\eta_L$ even with deeper mantle melting at higher T_p, facilitating the operation of plate tectonics in the early Earth.

[49] Though previous attempts to estimate the heat flow scaling of plate tectonics [*Korenaga*, 2003, 2006] have already predicted the inverse relation between mantle temperature and surface heat flux as indicated by Figure 8, there are a few important differences. First, because the effect of shallow stiffening eventually saturates (equation (44)), the inverse relation is restricted to a certain temperature range. This subtle behavior is difficult to derive from the global energy balance approach adopted by the previous studies. Second, the global energy balance can be exploited to derive heat flow scaling by *assuming* the mode of convection, so whether plate tectonic convection is plausible or not cannot be addressed. Finally, the energy balance approach has a few poorly constrained parameters, such as the radius of curvature for plate bending, effective lithospheric viscosity, and the aspect ratio of convection, and it is possible to obtain wildly different results by varying them independently [e.g., *Davies*, 2009]. Though similarly suffering from parameter uncertainty (e.g., γ and $\Delta\eta$) and from the very assumption of the pseudoplastic rheology as well, the present study provides a fully dynamic framework in which heat flow, velocity, lithospheric viscosity, aspect ratio, and the radius of curvature are all connected in a self-consistent manner.

Appendix A: Numerical Results

[50] Tabulated are selected convection diagnostics for statistically steady state solutions as described in the main text. The Rayleigh number Ra is 10^6 for all cases. Reference runs refer to calculations with the standard pseudoplastic rheology, and runs with shallow stiffening refers to those with additional depth-dependent viscosity (Tables A1–A8).

Table A1. Numerical Results for Reference Runs for $\gamma < 0.5$

γ	θ_0	H^*	$T^*_{\max}$	T_i^*	$\langle T^* \rangle$	Nu	θ	Ra_i	$v^*_{\rm rms}$	v_s^*	$P_{0.1}$	Φ	Φ_δ/Φ
0.1	15	8	0.86	0.59	0.60	9.27	12.9	1.10×10^5	6.40×10^1	1.49×10^2	0.33	2.73×10^7	0.19
0.1	15	12	0.93	0.68	0.69	12.93	13.9	3.18×10^5	1.12×10^2	2.26×10^2	0.30	4.25×10^7	0.14
0.1	15	16	0.98	0.75	0.76	16.39	14.6	6.85×10^5	1.68×10^2	3.10×10^2	0.26	5.77×10^7	0.13
0.1	15	20	1.02	0.82	0.81	19.67	15.3	1.32×10^6	2.33×10^2	3.97×10^2	0.22	7.31×10^7	0.14
0.1	20	12	0.96	0.71	0.70	12.50	19.2	4.36×10^5	1.00×10^2	2.22×10^2	0.27	4.22×10^7	0.16
0.1	20	16	1.00	0.77	0.77	15.95	20.1	1.08×10^6	1.57×10^2	3.18×10^2	0.28	5.77×10^7	0.13
0.1	20	20	1.04	0.84	0.82	19.28	20.8	2.21×10^6	2.19×10^2	4.02×10^2	0.25	7.30×10^7	0.13
0.1	25	12	0.97	0.74	0.70	12.32	24.4	5.15×10^5	8.78×10^1	2.13×10^2	0.22	4.19×10^7	0.16
0.1	25	16	1.02	0.80	0.77	15.69	25.5	1.68×10^6	1.43×10^2	3.01×10^2	0.27	5.73×10^7	0.14
0.1	25	20	1.05	0.85	0.82	19.04	26.3	3.74×10^6	2.06×10^2	3.97×10^2	0.28	7.28×10^7	0.13
0.2	15	8	0.94	0.66	0.66	8.48	14.2	4.05×10^5	5.97×10^1	1.11×10^2	0.45	2.67×10^7	0.23
0.2	15	12	1.00	0.74	0.75	12.04	15.0	9.57×10^5	1.21×10^2	2.06×10^2	0.48	4.20×10^7	0.17
0.2	15	16	1.04	0.79	0.81	15.37	15.6	1.93×10^6	1.94×10^2	3.20×10^2	0.49	5.75×10^7	0.16
0.2	15	20	1.08	0.83	0.86	18.55	16.2	3.49×10^6	2.72×10^2	4.26×10^2	0.48	7.30×10^7	0.17
0.2	20	8	0.98	0.72	0.68	8.14	19.7	6.97×10^5	4.61×10^1	9.66×10^1	0.39	2.62×10^7	0.23
0.2	20	12	1.05	0.78	0.76	11.49	20.9	2.58×10^6	1.08×10^2	1.99×10^2	0.49	4.17×10^7	0.18
0.2	20	16	1.07	0.83	0.81	14.98	21.4	4.18×10^6	1.76×10^2	3.06×10^2	0.49	5.72×10^7	0.16
0.2	20	20	1.10	0.87	0.86	18.24	21.9	7.57×10^6	2.70×10^2	4.57×10^2	0.52	7.28×10^7	0.16
0.2	25	8	0.98	0.78	0.67	8.13	24.6	6.69×10^5	4.13×10^1	1.06×10^2	0.25	2.58×10^7	0.25
0.2	25	12	1.05	0.83	0.77	11.43	26.3	3.73×10^6	9.51×10^1	1.82×10^2	0.45	4.11×10^7	0.18
0.2	25	16	1.09	0.87	0.82	14.69	27.2	1.02×10^7	1.76×10^2	3.10×10^2	0.52	5.64×10^7	0.16
0.2	25	20	1.11	0.90	0.86	18.08	27.7	1.59×10^7	2.53×10^2	4.34×10^2	0.52	7.18×10^7	0.16
0.3	15	8	1.02	0.68	0.71	7.83	15.3	1.43×10^6	6.27×10^1	1.02×10^2	0.64	2.65×10^7	0.26
0.3	15	12	1.04	0.75	0.77	11.54	15.6	1.90×10^6	1.35×10^2	2.19×10^2	0.56	4.20×10^7	0.21
0.3	15	16	1.08	0.80	0.83	14.79	16.2	3.70×10^6	2.15×10^2	3.44×10^2	0.58	5.75×10^7	0.19
0.3	15	20	1.13	0.84	0.89	17.73	16.9	7.76×10^6	3.38×10^2	5.42×10^2	0.61	7.30×10^7	0.20
0.3	20	8	1.02	0.76	0.70	7.81	20.5	1.68×10^6	4.90×10^1	8.94×10^1	0.45	2.61×10^7	0.29
0.3	20	12	1.08	0.81	0.79	11.08	21.7	5.80×10^6	1.34×10^2	2.23×10^2	0.60	4.14×10^7	0.22
0.3	20	16	1.12	0.84	0.84	14.29	22.4	1.25×10^7	2.20×10^2	3.65×10^2	0.63	5.71×10^7	0.19
0.3	20	20	1.14	0.87	0.88	17.53	22.8	1.94×10^7	3.20×10^2	5.26×10^2	0.63	7.27×10^7	0.19
0.3	25	8	1.04	0.82	0.72	7.66	26.1	3.17×10^6	5.10×10^1	9.93×10^1	0.42	2.54×10^7	0.30
0.3	25	12	1.09	0.85	0.80	11.03	27.2	9.97×10^6	1.15×10^2	1.91×10^2	0.55	4.05×10^7	0.23
0.3	25	16	1.13	0.88	0.85	14.18	28.2	2.82×10^7	2.19×10^2	3.49×10^2	0.63	5.55×10^7	0.20
0.3	25	20	1.16	0.91	0.90	17.22	29.1	6.71×10^7	3.76×10^2	5.84×10^2	0.68	7.08×10^7	0.21
0.4	15	8	1.04	0.68	0.72	7.67	15.6	1.99×10^6	5.32×10^1	8.93×10^1	0.55	2.66×10^7	0.32
0.4	15	12	1.07	0.77	0.80	11.20	16.1	3.18×10^6	1.59×10^2	2.50×10^2	0.63	4.19×10^7	0.24
0.4	15	16	1.11	0.81	0.85	14.39	16.7	6.03×10^6	2.43×10^2	3.89×10^2	0.63	5.74×10^7	0.21
0.4	15	20	1.16	0.84	0.90	17.23	17.4	1.31×10^7	3.63×10^2	5.79×10^2	0.67	7.31×10^7	0.22
0.4	20	8	1.06	0.79	0.74	7.56	21.2	3.43×10^6	5.36×10^1	7.34×10^1	0.52	2.57×10^7	0.34
0.4	20	12	1.11	0.83	0.82	10.80	22.2	1.04×10^7	1.56×10^2	2.38×10^2	0.64	4.13×10^7	0.25
0.4	20	16	1.16	0.86	0.89	13.81	23.2	2.81×10^7	3.03×10^2	4.55×10^2	0.72	5.71×10^7	0.24
0.4	20	20	1.20	0.89	0.93	16.75	23.9	5.92×10^7	4.43×10^2	6.68×10^2	0.73	7.25×10^7	0.25
0.4	25	8	1.09	0.84	0.75	7.37	27.1	9.21×10^6	5.96×10^1	1.00×10^2	0.45	2.52×10^7	0.36
0.4	25	12	1.11	0.87	0.84	10.81	27.8	1.75×10^7	1.67×10^2	2.26×10^2	0.61	3.92×10^7	0.27
0.4	25	16	1.16	0.90	0.90	13.76	29.1	6.93×10^7	3.08×10^2	4.16×10^2	0.71	5.44×10^7	0.25
0.4	25	20	1.21	0.92	0.95	16.61	30.1	2.05×10^8	4.94×10^2	6.45×10^2	0.72	6.88×10^7	0.28

Table A2. Numerical Results for Reference Runs for $\gamma > 0.5$

γ	θ_0	H^*	$T^*_{\max}$	T_i^*	$\langle T^* \rangle$	Nu	θ	Ra_i	$v^*_{\rm rms}$	v_s^*	$P_{0.1}$	Φ	Φ_δ/Φ
0.6	10	8	0.95	0.64	0.70	8.39	9.5	6.05×10^5	9.53×10^1	1.36×10^2	0.51	2.68×10^7	0.34
0.6	10	12	1.04	0.71	0.79	11.55	10.4	1.54×10^6	1.66×10^2	2.41×10^2	0.56	4.23×10^7	0.29
0.6	10	16	1.10	0.76	0.86	14.52	11.0	3.07×10^6	2.42×10^2	3.56×10^2	0.56	5.78×10^7	0.28
0.6	10	20	1.16	0.80	0.92	17.31	11.6	5.50×10^6	3.15×10^2	4.63×10^2	0.55	7.34×10^7	0.28
0.6	15	8	1.10	0.74	0.76	7.29	16.5	4.76×10^6	6.65×10^1	1.03×10^2	0.36	2.61×10^7	0.45
0.6	15	12	1.13	0.79	0.85	10.60	17.0	8.32×10^6	1.92×10^2	2.90×10^2	0.69	4.17×10^7	0.30
0.6	15	16	1.18	0.82	0.90	13.60	17.7	1.69×10^7	2.84×10^2	4.39×10^2	0.71	5.71×10^7	0.26
0.6	15	20	1.22	0.85	0.95	16.35	18.4	3.52×10^7	3.93×10^2	5.96×10^2	0.71	7.31×10^7	0.27
0.6	20	8	1.13	0.83	0.79	7.10	22.5	1.42×10^7	6.93×10^1	8.92×10^1	0.50	2.54×10^7	0.43
0.6	20	12	1.40	1.38	1.28	8.59	27.9	3.91×10^9	5.16×10^3	9.91×10^{-2}	0.00	3.41×10^7	0.35
0.6	20	16	1.21	0.88	0.94	13.20	24.3	8.69×10^7	3.52×10^2	4.85×10^2	0.68	5.63×10^7	0.31
0.6	20	20	1.26	0.89	0.98	15.85	25.3	2.45×10^8	5.01×10^2	7.14×10^2	0.66	7.19×10^7	0.32
0.8	10	8	1.09	0.64	0.79	7.34	10.9	2.66×10^6	1.05×10^2	1.57×10^2	0.73	2.69×10^7	0.33
0.8	10	12	1.07	0.72	0.82	11.17	10.7	2.28×10^6	1.70×10^2	2.48×10^2	0.58	4.23×10^7	0.32
0.8	10	16	1.14	0.76	0.88	14.06	11.4	4.53×10^6	2.44×10^2	3.64×10^2	0.58	5.78×10^7	0.30
0.8	10	20	1.20	0.80	0.94	16.66	12.0	8.97×10^6	3.30×10^2	5.00×10^2	0.59	7.36×10^7	0.29
0.8	15	8	1.14	0.77	0.79	7.03	17.1	8.92×10^6	7.00×10^1	9.55×10^1	0.33	2.58×10^7	0.50
0.8	15	12	1.18	0.81	0.89	10.22	17.6	1.63×10^7	1.93×10^2	2.89×10^2	0.64	4.13×10^7	0.32
0.8	15	16	1.23	0.84	0.95	13.01	18.5	3.90×10^7	2.98×10^2	4.43×10^2	0.66	5.74×10^7	0.31
0.8	15	20	1.28	0.86	1.00	15.59	19.3	9.11×10^7	4.17×10^2	6.27×10^2	0.66	7.32×10^7	0.32
0.8	20	8	1.32	1.30	1.18	6.04	26.5	8.79×10^8	1.79×10^3	4.93×10^{-3}	0.00	2.06×10^7	0.42
0.8	20	12	1.24	0.88	0.94	9.69	24.8	1.47×10^8	2.59×10^2	2.90×10^2	0.50	4.04×10^7	0.36
0.8	20	16	1.29	0.89	1.00	12.38	25.9	4.51×10^8	4.25×10^2	5.07×10^2	0.53	5.53×10^7	0.34
0.8	20	20	1.35	0.90	1.05	14.84	27.0	1.42×10^9	6.75×10^2	7.17×10^2	0.52	7.15×10^7	0.31
1.0	10	8	1.10	0.64	0.79	7.30	11.0	2.85×10^6	1.00×10^2	1.52×10^2	0.60	2.69×10^7	0.39
1.0	10	12	1.11	0.72	0.84	10.84	11.1	3.29×10^6	1.67×10^2	2.50×10^2	0.58	4.24×10^7	0.34
1.0	10	16	1.17	0.76	0.91	13.64	11.7	6.67×10^6	2.48×10^2	3.80×10^2	0.60	5.80×10^7	0.31
1.0	10	20	1.23	0.79	0.96	16.21	12.3	1.29×10^7	3.21×10^2	5.02×10^2	0.60	7.38×10^7	0.30
1.0	15	8	1.19	0.86	0.84	6.74	17.8	1.94×10^7	1.13×10^2	1.32×10^2	0.27	2.52×10^7	0.55
1.0	15	12	1.24	0.83	0.91	9.65	18.7	4.80×10^7	1.86×10^2	2.79×10^2	0.43	4.14×10^7	0.40
1.0	15	16	1.51	1.49	1.40	10.61	22.6	3.08×10^9	6.13×10^3	4.93×10^{-1}	0.00	4.89×10^7	0.30
1.0	15	20	1.52	1.50	1.42	13.18	22.8	3.58×10^9	8.31×10^3	1.55×10^{-1}	0.00	6.32×10^7	0.29
1.0	20	8	1.33	1.31	1.19	6.04	26.5	8.89×10^8	1.89×10^3	6.51×10^{-3}	0.00	2.07×10^7	0.43
1.0	20	12	1.39	1.38	1.28	8.61	27.9	3.72×10^9	4.71×10^3	4.37×10^{-3}	0.00	3.41×10^7	0.34
1.0	20	16	1.41	1.40	1.31	11.38	28.1	4.76×10^9	7.85×10^3	7.17×10^{-3}	0.00	4.82×10^7	0.31
1.0	20	20	1.46	1.45	1.38	13.69	29.2	1.49×10^{10}	1.57×10^4	2.07×10^{-3}	0.00	6.30×10^7	0.24

Table A3. Numerical Results With Shallow Stiffening for $\gamma = 0.4$, $\theta_0 = 15$, and $H^* > 7$

θ_0	H^*	h^*	$\Delta\eta$	$T^*_{\max}$	$\langle T^* \rangle$	Nu	θ	Ra_i	$v^*_{\rm rms}$	v^*_s	$P_{0.1}$	Φ	Φ_δ/Φ
15	8	0.1	3	1.08	0.73	7.43	16.1	3.38×10^6	6.49×10^1	1.10×10^2	0.59	2.64×10^7	0.38
15	8	0.1	10	1.06	0.75	7.53	15.9	2.74×10^6	6.67×10^1	9.24×10^1	0.71	2.62×10^7	0.33
15	8	0.1	30	1.05	0.75	7.62	15.8	2.28×10^6	7.51×10^1	1.10×10^2	0.69	2.62×10^7	0.33
15	8	0.1	100	1.07	0.75	7.49	16.0	3.01×10^6	7.62×10^1	1.13×10^2	0.67	2.62×10^7	0.33
15	8	0.2	3	1.05	0.76	7.63	15.7	2.22×10^6	9.88×10^1	1.41×10^2	0.65	2.60×10^7	0.33
15	8	0.2	10	1.08	0.79	7.40	16.2	3.69×10^6	1.07×10^2	1.43×10^2	0.71	2.59×10^7	0.33
15	8	0.2	30	1.11	0.82	7.23	16.6	5.57×10^6	1.11×10^2	1.39×10^2	0.78	2.58×10^7	0.31
15	8	0.2	100	1.15	0.87	6.94	17.3	1.15×10^7	1.15×10^2	1.31×10^2	0.84	2.57×10^7	0.28
15	8	0.3	3	1.07	0.77	7.47	16.1	3.18×10^6	9.47×10^1	1.34×10^2	0.62	2.59×10^7	0.34
15	8	0.3	10	1.11	0.81	7.21	16.7	5.80×10^6	1.05×10^2	1.34×10^2	0.65	2.59×10^7	0.34
15	8	0.3	30	1.15	0.85	6.98	17.2	1.03×10^7	1.07×10^2	1.27×10^2	0.65	2.58×10^7	0.34
15	12	0.1	3	1.08	0.80	11.13	16.2	3.50×10^6	1.65×10^2	2.55×10^2	0.65	4.18×10^7	0.25
15	12	0.1	10	1.10	0.82	10.94	16.5	4.77×10^6	1.89×10^2	2.87×10^2	0.69	4.16×10^7	0.26
15	12	0.1	30	1.10	0.83	10.87	16.6	5.29×10^6	1.87×10^2	2.79×10^2	0.71	4.16×10^7	0.26
15	12	0.1	100	1.12	0.85	10.74	16.8	6.54×10^6	1.89×10^2	2.73×10^2	0.74	4.14×10^7	0.27
15	12	0.2	3	1.11	0.83	10.86	16.6	5.42×10^6	1.91×10^2	2.82×10^2	0.67	4.16×10^7	0.26
15	12	0.2	10	1.15	0.88	10.45	17.2	1.07×10^7	1.96×10^2	2.69×10^2	0.71	4.16×10^7	0.27
15	12	0.2	30	1.58	1.43	7.58	23.7	9.82×10^9	8.13×10^3	1.57×10^{-2}	0.00	3.09×10^7	0.36
15	12	0.3	3	1.12	0.84	10.70	16.8	7.07×10^6	1.82×10^2	2.62×10^2	0.68	4.17×10^7	0.26
15	12	0.3	10	1.18	0.90	10.17	17.7	1.78×10^7	1.89×10^2	2.49×10^2	0.71	4.16×10^7	0.27
15	12	0.3	30	1.21	0.93	9.89	18.2	3.03×10^7	1.88×10^2	2.32×10^2	0.71	4.15×10^7	0.29
15	16	0.1	3	1.13	0.87	14.11	17.0	8.58×10^6	2.76×10^2	4.31×10^2	0.68	5.74×10^7	0.23
15	16	0.1	10	1.15	0.89	13.86	17.3	1.18×10^7	2.92×10^2	4.43×10^2	0.72	5.74×10^7	0.24
15	16	0.1	30	1.17	0.91	13.63	17.6	1.62×10^7	2.92×10^2	4.24×10^2	0.75	5.72×10^7	0.25
15	16	0.1	100	1.21	0.95	13.28	18.1	2.70×10^7	4.25×10^2	3.76×10^2	0.76	5.63×10^7	0.27
15	16	0.2	3	1.16	0.89	13.77	17.4	1.34×10^7	2.98×10^2	4.41×10^2	0.69	5.74×10^7	0.24
15	16	0.2	10	1.21	0.94	13.22	18.2	2.87×10^7	3.02×10^2	4.16×10^2	0.71	5.73×10^7	0.26
15	16	0.2	30	1.25	0.97	12.83	18.7	5.15×10^7	2.97×10^2	3.82×10^2	0.73	5.71×10^7	0.28
15	16	0.2	100	1.30	1.02	12.28	19.6	1.25×10^8	3.11×10^2	3.80×10^2	0.72	5.71×10^7	0.29
15	16	0.3	3	1.18	0.91	13.53	17.8	1.86×10^7	2.95×10^2	4.23×10^2	0.72	5.73×10^7	0.24
15	16	0.3	10	1.24	0.96	12.96	18.5	4.21×10^7	2.81×10^2	3.64×10^2	0.74	5.73×10^7	0.27
15	16	0.3	30	1.28	0.99	12.47	19.3	9.10×10^7	2.84×10^2	3.46×10^2	0.75	5.72×10^7	0.28
15	16	0.3	100	1.33	1.03	12.04	20.0	1.89×10^8	2.86×10^2	3.25×10^2	0.74	5.69×10^7	0.29
15	20	0.1	3	1.18	0.93	16.89	17.8	1.89×10^7	3.89×10^2	6.00×10^2	0.70	7.31×10^7	0.23
15	20	0.1	10	1.21	0.95	16.55	18.1	2.79×10^7	3.87×10^2	5.70×10^2	0.73	7.30×10^7	0.25
15	20	0.1	100	1.27	1.00	15.81	19.0	6.82×10^7	3.94×10^2	5.42×10^2	0.78	7.29×10^7	0.28
15	20	0.2	3	1.21	0.95	16.53	18.2	2.85×10^7	3.93×10^2	5.73×10^2	0.70	7.31×10^7	0.25
15	20	0.2	10	1.25	0.99	15.96	18.8	5.70×10^7	3.99×10^2	5.35×10^2	0.71	7.30×10^7	0.27
15	20	0.2	30	1.30	1.02	15.45	19.4	1.08×10^8	3.99×10^2	5.12×10^2	0.72	7.29×10^7	0.28
15	20	0.3	3	1.22	0.96	16.40	18.3	3.34×10^7	3.80×10^2	5.36×10^2	0.71	7.30×10^7	0.25
15	20	0.3	10	1.28	1.01	15.67	19.2	8.20×10^7	3.78×10^2	4.85×10^2	0.73	7.29×10^7	0.28
15	20	0.3	30	1.33	1.05	15.07	19.9	1.83×10^8	3.94×10^2	4.69×10^2	0.74	7.27×10^7	0.30
15	20	0.3	100	1.39	1.09	14.36	20.9	5.13×10^8	4.03×10^2	4.53×10^2	0.76	7.25×10^7	0.30

Table A4. Numerical Results With Shallow Stiffening for $\gamma = 0.4$, $\theta_0 = 20$, and $H^* > 7$

θ_0	H^*	h^*	$\Delta\eta$	T^*_{max}	$\langle T^* \rangle$	Nu	θ	Ra_i	v^*_{rms}	v^*_s	$P_{0.1}$	Φ	Φ_δ/Φ
20	8	0.1	3	1.06	0.74	7.52	21.3	3.80×10^6	5.14×10^1	7.50×10^1	0.51	2.58×10^7	0.34
20	8	0.1	10	1.08	0.74	7.42	21.6	5.10×10^6	5.77×10^1	9.57×10^1	0.50	2.57×10^7	0.37
20	8	0.1	30	1.09	0.75	7.32	21.9	7.02×10^6	5.60×10^1	9.39×10^1	0.49	2.56×10^7	0.38
20	8	0.1	100	1.12	0.76	7.11	22.5	1.37×10^7	5.59×10^1	8.57×10^1	0.52	2.52×10^7	0.38
20	8	0.2	3	1.10	0.75	7.28	22.0	7.94×10^6	5.74×10^1	9.07×10^1	0.47	2.57×10^7	0.37
20	8	0.2	10	1.13	0.78	7.08	22.6	1.52×10^7	5.34×10^1	7.60×10^1	0.50	2.57×10^7	0.34
20	8	0.2	30	1.14	0.81	7.02	22.8	1.89×10^7	7.63×10^1	9.28×10^1	0.63	2.53×10^7	0.33
20	8	0.3	3	1.10	0.76	7.29	22.0	7.81×10^6	5.88×10^1	9.37×10^1	0.48	2.57×10^7	0.37
20	8	0.3	10	1.13	0.80	7.06	22.7	1.62×10^7	6.88×10^1	9.41×10^1	0.53	2.54×10^7	0.36
20	8	0.3	30	1.15	0.85	6.95	23.0	2.42×10^7	1.17×10^2	1.30×10^2	0.62	2.48×10^7	0.36
20	8	0.3	100	1.20	0.90	6.69	23.9	6.19×10^7	1.32×10^2	1.24×10^2	0.65	2.45×10^7	0.34
20	12	0.1	3	1.12	0.82	10.74	22.4	1.18×10^7	1.50×10^2	2.32×10^2	0.65	4.12×10^7	0.26
20	12	0.1	10	1.13	0.84	10.65	22.5	1.44×10^7	1.77×10^2	2.58×10^2	0.69	4.08×10^7	0.27
20	12	0.1	30	1.14	0.86	10.56	22.7	1.75×10^7	2.01×10^2	2.72×10^2	0.72	4.02×10^7	0.28
20	12	0.1	100	1.15	0.89	10.42	23.1	2.47×10^7	2.03×10^2	2.48×10^2	0.74	3.97×10^7	0.29
20	12	0.2	3	1.14	0.86	10.54	22.8	1.85×10^7	2.05×10^2	2.86×10^2	0.70	4.09×10^7	0.27
20	12	0.2	10	1.17	0.89	10.30	23.3	3.22×10^7	2.23×10^2	2.86×10^2	0.72	4.05×10^7	0.29
20	12	0.2	30	1.19	0.92	10.08	23.8	5.51×10^7	2.33×10^2	2.68×10^2	0.75	4.03×10^7	0.32
20	12	0.3	3	1.15	0.86	10.43	23.0	2.36×10^7	1.96×10^2	2.74×10^2	0.69	4.09×10^7	0.28
20	12	0.3	10	1.18	0.90	10.18	23.6	4.26×10^7	2.05×10^2	2.57×10^2	0.71	4.06×10^7	0.29
20	12	0.3	30	1.21	0.93	9.91	24.2	8.38×10^7	2.13×10^2	2.46×10^2	0.71	4.03×10^7	0.31
20	12	0.3	100	1.25	0.96	9.59	25.0	1.94×10^8	2.19×10^2	2.30×10^2	0.71	3.94×10^7	0.33
20	16	0.1	3	1.17	0.89	13.73	23.3	3.22×10^7	3.15×10^2	4.66×10^2	0.73	5.66×10^7	0.25
20	16	0.1	10	1.17	0.91	13.64	23.5	3.79×10^7	3.22×10^2	4.48×10^2	0.75	5.61×10^7	0.26
20	16	0.1	30	1.18	0.92	13.54	23.6	4.52×10^7	3.27×10^2	4.28×10^2	0.75	5.55×10^7	0.28
20	16	0.1	100	1.21	0.95	13.19	24.3	8.75×10^7	3.38×10^2	4.03×10^2	0.78	5.50×10^7	0.29
20	16	0.2	3	1.18	0.91	13.52	23.7	4.69×10^7	3.31×10^2	4.62×10^2	0.72	5.66×10^7	0.26
20	16	0.2	10	1.22	0.95	13.18	24.3	8.98×10^7	3.47×10^2	4.38×10^2	0.74	5.61×10^7	0.29
20	16	0.2	30	1.25	0.98	12.81	25.0	1.87×10^8	3.64×10^2	4.34×10^2	0.74	5.58×10^7	0.31
20	16	0.2	100	1.29	1.02	12.41	25.8	4.24×10^8	3.82×10^2	3.94×10^2	0.73	5.55×10^7	0.34
20	16	0.3	3	1.19	0.92	13.46	23.8	5.27×10^7	3.15×10^2	4.38×10^2	0.72	5.64×10^7	0.26
20	16	0.3	10	1.23	0.96	13.00	24.6	1.26×10^8	3.23×10^2	4.01×10^2	0.74	5.60×10^7	0.28
20	16	0.3	30	1.27	0.99	12.60	25.4	2.89×10^8	3.32×10^2	3.80×10^2	0.75	5.58×10^7	0.30
20	16	0.3	100	1.31	1.02	12.23	26.2	6.45×10^8	3.34×10^2	3.47×10^2	0.75	5.55×10^7	0.32
20	20	0.1	3	1.21	0.95	16.54	24.2	8.04×10^7	4.53×10^2	6.49×10^2	0.75	7.23×10^7	0.27
20	20	0.1	10	1.22	0.96	16.37	24.5	1.05×10^8	4.65×10^2	6.32×10^2	0.77	7.18×10^7	0.28
20	20	0.1	100	1.29	1.01	15.48	25.9	4.59×10^8	4.89×10^2	6.44×10^2	0.82	7.06×10^7	0.27
20	20	0.2	3	1.23	0.96	16.30	24.6	1.17×10^8	4.66×10^2	6.42×10^2	0.74	7.22×10^7	0.28
20	20	0.2	10	1.26	0.99	15.88	25.2	2.31×10^8	4.70×10^2	5.94×10^2	0.74	7.19×10^7	0.30
20	20	0.2	30	1.30	1.02	15.42	26.0	5.07×10^8	4.90×10^2	5.88×10^2	0.74	7.17×10^7	0.31
20	20	0.2	100	1.35	1.06	14.88	26.9	1.34×10^9	5.16×10^2	5.64×10^2	0.74	7.13×10^7	0.31
20	20	0.3	3	1.23	0.97	16.25	24.6	1.28×10^8	4.44×10^2	6.03×10^2	0.74	7.22×10^7	0.28
20	20	0.3	10	1.28	1.00	15.68	25.5	3.27×10^8	4.45×10^2	5.51×10^2	0.76	7.18×10^7	0.29
20	20	0.3	100	1.36	1.06	14.78	27.1	1.65×10^9	4.59×10^2	4.78×10^2	0.76	7.13×10^7	0.33

Table A5. Numerical Results With Shallow Stiffening for $\gamma = 0.4$, $\theta_0 = 25$, and $H^* > 7$

θ_0	H^*	h^*	$\Delta\eta$	T^*_{max}	$\langle T^* \rangle$	Nu	θ	Ra_i	v^*_{rms}	v^*_s	$P_{0.1}$	Φ	Φ_δ/Φ
25	8	0.1	3	1.09	0.76	7.37	27.1	9.32×10^6	6.88×10^1	1.07×10^2	0.49	2.46×10^7	0.36
25	8	0.1	10	1.29	1.16	6.20	32.3	1.86×10^9	2.99×10^3	6.71×10^{-4}	0.00	2.05×10^7	0.43
25	8	0.1	30	1.29	1.16	6.22	32.2	1.67×10^9	3.02×10^3	9.93×10^{-5}	0.00	2.06×10^7	0.43
25	8	0.1	100	1.11	0.80	7.20	27.8	1.87×10^7	8.04×10^1	9.53×10^1	0.55	2.40×10^7	0.34
25	8	0.2	3	1.11	0.77	7.22	27.7	1.69×10^7	6.59×10^1	9.62×10^1	0.49	2.48×10^7	0.36
25	8	0.2	10	1.14	0.80	7.00	28.6	4.12×10^7	7.04×10^1	9.08×10^1	0.54	2.45×10^7	0.35
25	8	0.2	30	1.20	0.86	6.66	30.0	1.84×10^8	1.00×10^2	6.78×10^1	0.47	2.47×10^7	0.32
25	8	0.2	100	1.20	0.88	6.70	29.9	1.60×10^8	1.62×10^2	8.69×10^1	0.66	2.35×10^7	0.32
25	8	0.3	3	1.10	0.78	7.25	27.6	1.46×10^7	6.60×10^1	9.81×10^1	0.49	2.46×10^7	0.36
25	12	0.1	3	1.13	0.84	10.60	28.3	3.10×10^7	1.42×10^2	2.11×10^2	0.62	3.93×10^7	0.28
25	12	0.1	10	1.14	0.85	10.50	28.6	4.14×10^7	1.60×10^2	2.19×10^2	0.66	3.88×10^7	0.28
25	12	0.1	30	1.16	0.89	10.34	29.0	6.60×10^7	2.09×10^2	2.34×10^2	0.72	3.80×10^7	0.28
25	12	0.3	3	1.15	0.86	10.42	28.8	5.22×10^7	1.72×10^2	2.28×10^2	0.66	3.90×10^7	0.28
25	12	0.3	10	1.18	0.90	10.14	29.6	1.20×10^8	2.12×10^2	2.42×10^2	0.70	3.79×10^7	0.31
25	16	0.1	30	1.22	0.95	13.09	30.6	3.33×10^8	3.71×10^2	4.17×10^2	0.76	5.42×10^7	0.28
25	16	0.2	3	1.19	0.93	13.41	29.8	1.52×10^8	3.62×10^2	4.41×10^2	0.74	5.32×10^7	0.28
25	16	0.2	10	1.22	0.96	13.12	30.5	3.08×10^8	3.86×10^2	4.11×10^2	0.74	5.72×10^7	0.29
25	16	0.3	10	1.23	0.96	13.04	30.7	3.72×10^8	6.10×10^2	4.00×10^2	0.76	7.53×10^7	0.37
25	20	0.1	3	1.22	0.96	16.35	30.6	3.38×10^8	5.04×10^2	6.82×10^2	0.76	6.81×10^7	0.27
25	20	0.1	10	1.25	0.97	15.96	31.4	7.30×10^8	5.22×10^2	7.03×10^2	0.78	6.79×10^7	0.27
25	20	0.1	30	1.30	0.97	15.33	32.6	2.64×10^9	4.88×10^2	7.25×10^2	0.77	7.06×10^7	0.22
25	20	0.1	100	1.35	1.06	14.77	33.9	9.60×10^9	1.28×10^3	6.47×10^2	0.80	6.99×10^7	0.21

Table A6. Numerical Results With Shallow Stiffening for $\gamma = 0.4$, $\theta_0 = 15$, and $H^* < 7$

θ_0	H^*	h^*	$\Delta\eta$	T^*_{max}	$\langle T^* \rangle$	Nu	θ	Ra_i	v^*_{rms}	v^*_s	$P_{0.1}$	Φ	Φ_δ/Φ
15	2	0.1	3	0.82	0.51	2.44	12.3	5.59×10^4	7.67×10^0	5.19×10^0	0.15	2.44×10^6	0.88
15	2	0.1	10	0.82	0.51	2.44	12.3	5.59×10^4	7.67×10^0	5.18×10^0	0.20	2.44×10^6	0.88
15	2	0.1	30	0.82	0.51	2.44	12.3	5.59×10^4	7.67×10^0	5.17×10^0	0.25	2.44×10^6	0.88
15	2	0.1	100	0.82	0.51	2.44	12.3	5.59×10^4	7.67×10^0	5.19×10^0	0.27	2.44×10^6	0.88
15	2	0.2	3	0.83	0.52	2.41	12.4	6.44×10^4	7.88×10^0	4.85×10^0	0.35	2.42×10^6	0.88
15	2	0.2	10	0.84	0.52	2.38	12.6	7.50×10^4	8.17×10^0	4.80×10^0	0.35	2.54×10^6	0.88
15	2	0.2	30	0.84	0.52	2.38	12.6	7.70×10^4	8.20×10^0	4.75×10^0	0.45	2.54×10^6	0.87
15	2	0.2	100	0.84	0.52	2.38	12.6	7.74×10^4	8.21×10^0	4.74×10^0	0.52	2.55×10^6	0.87
15	2	0.3	3	0.85	0.52	2.36	12.7	8.78×10^4	8.27×10^0	4.55×10^0	0.38	2.50×10^6	0.87
15	2	0.3	10	0.86	0.54	2.31	13.0	1.13×10^5	8.76×10^0	3.94×10^0	0.46	2.36×10^6	0.89
15	2	0.3	30	0.91	0.63	2.19	13.7	2.54×10^5	1.18×10^1	4.22×10^{-3}	0.00	1.17×10^6	0.87
15	2	0.3	100	0.91	0.63	2.19	13.7	2.55×10^5	1.18×10^1	1.24×10^{-3}	0.00	1.16×10^6	0.87
15	4	0.1	3	0.90	0.60	4.42	13.6	2.16×10^5	2.28×10^1	2.60×10^1	0.50	1.07×10^7	0.52
15	4	0.1	10	0.91	0.60	4.42	13.6	2.19×10^5	2.28×10^1	2.59×10^1	0.45	1.07×10^7	0.52
15	4	0.1	30	0.91	0.60	4.40	13.6	2.34×10^5	2.28×10^1	2.59×10^1	0.54	1.07×10^7	0.52
15	4	0.1	100	0.91	0.60	4.40	13.7	2.36×10^5	2.28×10^1	2.59×10^1	0.55	1.07×10^7	0.51
15	4	0.2	3	0.91	0.61	4.38	13.7	2.49×10^5	2.26×10^1	2.50×10^1	0.48	1.07×10^7	0.49
15	4	0.2	10	0.95	0.62	4.23	14.2	4.22×10^5	2.58×10^1	2.98×10^1	0.44	1.05×10^7	0.52
15	4	0.2	30	0.94	0.63	4.23	14.2	4.12×10^5	2.54×10^1	2.53×10^1	0.70	1.05×10^7	0.48
15	4	0.2	100	0.95	0.64	4.19	14.3	4.85×10^5	2.58×10^1	2.45×10^1	0.71	1.05×10^7	0.48
15	4	0.3	3	0.92	0.62	4.33	13.9	2.95×10^5	2.28×10^1	2.35×10^1	0.46	1.06×10^7	0.48
15	4	0.3	10	0.94	0.65	4.24	14.2	4.09×10^5	2.33×10^1	2.12×10^1	0.65	1.05×10^7	0.46
15	4	0.3	30	0.96	0.67	4.17	14.4	5.25×10^5	2.41×10^1	1.99×10^1	0.55	1.04×10^7	0.46
15	4	0.3	100	0.99	0.69	4.06	14.8	8.02×10^5	2.62×10^1	2.05×10^1	0.54	1.02×10^7	0.49
15	6	0.1	3	0.99	0.67	6.07	14.8	8.22×10^5	3.67×10^1	5.24×10^1	0.62	1.86×10^7	0.39
15	6	0.1	10	0.99	0.68	6.05	14.9	8.74×10^5	3.65×10^1	5.15×10^1	0.65	1.86×10^7	0.38
15	6	0.1	30	0.99	0.68	6.04	14.9	9.09×10^5	3.64×10^1	5.08×10^1	0.67	1.86×10^7	0.38
15	6	0.1	100	1.02	0.68	5.89	15.3	1.34×10^6	3.91×10^1	5.51×10^1	0.60	1.85×10^7	0.40
15	6	0.2	3	1.00	0.69	6.02	15.0	9.50×10^5	3.66×10^1	4.95×10^1	0.66	1.86×10^7	0.36
15	6	0.2	10	1.03	0.71	5.80	15.5	1.73×10^6	4.14×10^1	5.46×10^1	0.71	1.84×10^7	0.35
15	6	0.2	30	1.06	0.74	5.65	15.9	2.72×10^6	4.60×10^1	5.43×10^1	0.75	1.83×10^7	0.33
15	6	0.2	100	1.10	0.77	5.45	16.5	5.06×10^6	5.91×10^1	6.26×10^1	0.82	1.80×10^7	0.35
15	6	0.3	3	1.01	0.70	5.93	15.2	1.21×10^6	3.65×10^1	4.78×10^1	0.66	1.85×10^7	0.37
15	6	0.3	10	1.08	0.76	5.57	16.2	3.40×10^6	4.68×10^1	5.33×10^1	0.59	1.81×10^7	0.39
15	6	0.3	30	1.11	0.80	5.39	16.7	6.03×10^6	7.22×10^1	7.49×10^1	0.63	1.78×10^7	0.40
15	6	0.3	100	1.16	0.84	5.18	17.4	1.24×10^7	7.88×10^1	6.61×10^1	0.68	1.76×10^7	0.36

Table A7. Numerical Results With Shallow Stiffening for $\gamma = 0.4$, $\theta_0 = 20$ and 25, and $H^* < 7$

θ_0	H^*	h^*	$\Delta\eta$	T^*_{max}	$\langle T^* \rangle$	Nu	θ	Ra_i	v^*_{rms}	v^*_s	$P_{0.1}$	Φ	Φ_δ/Φ
20	2	0.1	3	0.96	0.65	2.08	19.3	4.62×10^5	9.88×10^0	2.53×10^{-3}	0.00	7.02×10^5	0.94
20	2	0.2	3	0.96	0.65	2.08	19.3	4.62×10^5	9.89×10^0	1.02×10^{-3}	0.00	7.02×10^5	0.94
20	2	0.3	3	0.96	0.65	2.08	19.3	4.66×10^5	9.90×10^0	8.63×10^{-4}	0.00	6.98×10^5	0.94
20	4	0.1	3	1.01	0.66	3.97	20.2	1.18×10^6	2.28×10^1	2.09×10^1	0.56	9.79×10^6	0.58
20	4	0.1	10	0.98	0.64	4.07	19.7	7.25×10^5	2.21×10^1	4.45×10^1	0.37	9.86×10^6	0.53
20	4	0.1	30	1.01	0.67	3.94	20.3	1.35×10^6	2.33×10^1	2.03×10^1	0.58	9.66×10^6	0.57
20	4	0.1	100	1.02	0.67	3.93	20.4	1.45×10^6	2.35×10^1	2.08×10^1	0.50	9.59×10^6	0.56
20	4	0.2	3	1.00	0.66	3.99	20.1	1.09×10^6	2.62×10^1	4.06×10^1	0.43	9.70×10^6	0.52
20	4	0.2	10	1.02	0.67	3.93	20.4	1.46×10^6	2.57×10^1	3.53×10^1	0.53	9.70×10^6	0.50
20	4	0.2	30	1.04	0.69	3.83	20.9	2.56×10^6	2.47×10^1	2.05×10^1	0.49	9.70×10^6	0.54
20	4	0.2	100	1.05	0.69	3.81	21.0	2.86×10^6	2.67×10^1	2.63×10^1	0.50	9.57×10^6	0.53
20	4	0.3	3	1.03	0.69	3.89	20.6	1.82×10^6	2.38×10^1	1.87×10^1	0.58	9.74×10^6	0.51
20	4	0.3	10	1.21	0.99	3.31	24.1	7.64×10^7	3.69×10^2	9.90×10^{-7}	0.00	6.30×10^6	0.60
20	6	0.1	3	1.05	0.71	5.73	20.9	2.66×10^6	3.78×10^1	4.56×10^1	0.49	1.78×10^7	0.41
20	6	0.1	10	1.04	0.70	5.78	20.8	2.28×10^6	3.73×10^1	5.86×10^1	0.45	1.78×10^7	0.43
20	6	0.1	30	1.07	0.72	5.63	21.3	3.99×10^6	3.48×10^1	4.54×10^1	0.52	1.77×10^7	0.40
20	6	0.1	100	1.08	0.72	5.58	21.5	4.85×10^6	3.58×10^1	5.00×10^1	0.46	1.76×10^7	0.43
20	6	0.2	3	1.06	0.71	5.65	21.2	3.66×10^6	3.35×10^1	4.62×10^1	0.46	1.78×10^7	0.42
20	6	0.2	10	1.09	0.73	5.51	21.8	6.55×10^6	3.72×10^1	4.73×10^1	0.53	1.77×10^7	0.42
20	6	0.2	30	1.09	0.74	5.51	21.8	6.36×10^6	4.24×10^1	5.40×10^1	0.62	1.76×10^7	0.41
20	6	0.2	100	1.13	0.78	5.31	22.6	1.51×10^7	4.90×10^1	4.60×10^1	0.68	1.74×10^7	0.37
20	6	0.3	3	1.07	0.72	5.63	21.3	3.93×10^6	3.78×10^1	5.60×10^1	0.42	1.77×10^7	0.46
20	6	0.3	10	1.11	0.76	5.42	22.1	9.33×10^6	3.96×10^1	4.84×10^1	0.45	1.76×10^7	0.42
20	6	0.3	30	1.14	0.79	5.27	22.8	1.80×10^7	4.60×10^1	4.96×10^1	0.57	1.74×10^7	0.37
20	6	0.3	100	1.43	1.21	4.20	28.6	7.48×10^9	3.65×10^3	1.97×10^{-8}	0.00	8.70×10^6	0.53
25	2	0.1	3	0.98	0.66	2.04	24.6	6.29×10^5	7.35×10^0	5.99×10^{-8}	0.00	3.93×10^5	0.96
25	2	0.2	3	0.98	0.66	2.04	24.6	6.29×10^5	7.35×10^0	5.48×10^{-8}	0.00	3.93×10^5	0.96
25	2	0.3	3	0.98	0.66	2.04	24.6	6.29×10^5	7.36×10^0	5.06×10^{-8}	0.00	3.93×10^5	0.96
25	4	0.1	3	1.17	0.97	3.41	29.3	8.56×10^7	3.90×10^2	8.75×10^{-6}	0.00	6.68×10^6	0.60
25	4	0.2	3	1.17	0.97	3.41	29.3	8.59×10^7	3.90×10^2	4.69×10^{-6}	0.00	6.66×10^6	0.60
25	4	0.3	3	1.19	0.98	3.36	29.7	1.33×10^8	4.66×10^2	4.88×10^{-8}	0.00	6.40×10^6	0.60
25	6	0.1	3	1.25	1.09	4.80	31.2	6.39×10^8	1.39×10^3	1.79×10^{-4}	0.00	1.36×10^7	0.49
25	6	0.2	3	1.25	1.09	4.79	31.3	7.05×10^8	1.23×10^3	2.44×10^{-5}	0.00	1.33×10^7	0.46
25	6	0.3	3	1.28	1.12	4.67	32.1	1.56×10^9	2.00×10^3	3.59×10^{-4}	0.00	1.31×10^7	0.50

Table A8. Numerical Results With Shallow Stiffening for $\gamma = 0.8$

θ_0	H^*	h^*	$\Delta\eta$	T^*_{max}	$\langle T^* \rangle$	Nu	θ	Ra_i	v^*_{rms}	v^*_s	$P_{0.1}$	Φ	Φ_δ/Φ
10	2	0.2	1000	0.85	0.58	2.35	8.5	1.91×10^5	1.79×10^1	3.66×10^{-2}	0.00	2.07×10^6	0.86
10	2	0.3	10	0.80	0.53	2.50	8.0	1.07×10^5	1.37×10^1	3.83×10^0	0.46	2.72×10^6	0.83
10	2	0.3	100	0.88	0.60	2.27	8.8	2.66×10^5	1.89×10^1	1.23×10^{-1}	0.00	1.75×10^6	0.87
10	3	0.2	10	0.75	0.52	3.98	7.5	6.49×10^4	2.01×10^1	1.77×10^1	0.66	7.61×10^6	0.63
10	3	0.2	100	1.00	0.78	2.99	10.0	1.03×10^6	5.80×10^1	4.43×10^{-2}	0.00	4.41×10^6	0.68
10	3	0.3	10	0.83	0.58	3.62	8.3	1.49×10^5	2.14×10^1	1.39×10^1	0.57	6.95×10^6	0.70
10	4	0.1	10	0.77	0.55	5.18	7.7	7.89×10^4	2.89×10^1	3.37×10^1	0.73	1.17×10^7	0.53
10	4	0.1	100	0.78	0.55	5.15	7.8	8.36×10^4	2.90×10^1	3.34×10^1	0.79	1.17×10^7	0.54
10	4	0.1	1000	0.78	0.55	5.15	7.8	8.38×10^4	2.90×10^1	3.33×10^1	0.79	1.17×10^7	0.54
10	4	0.2	10	0.82	0.59	4.90	8.2	1.31×10^5	3.11×10^1	3.14×10^1	0.59	1.14×10^7	0.58
10	4	0.2	100	1.11	0.92	3.61	11.1	3.26×10^6	1.13×10^2	7.14×10^{-3}	0.00	7.34×10^6	0.61
10	4	0.3	10	0.88	0.63	4.52	8.8	2.80×10^5	3.55×10^1	3.27×10^1	0.53	1.09×10^7	0.64
12	2	0.2	10	0.80	0.51	2.49	9.6	7.47×10^4	1.05×10^1	4.58×10^0	0.57	2.80×10^6	0.85
12	2	0.2	100	0.90	0.60	2.23	10.7	2.55×10^5	1.58×10^1	3.23×10^{-1}	0.00	1.70×10^6	0.91
12	2	0.3	10	0.90	0.61	2.22	10.8	2.79×10^5	1.59×10^1	6.30×10^{-1}	0.00	1.63×10^6	0.91
12	2	0.3	100	0.92	0.62	2.18	11.0	3.34×10^5	1.68×10^1	4.51×10^{-2}	0.00	1.46×10^6	0.93
12	3	0.1	10	0.82	0.54	3.68	9.8	8.91×10^4	1.79×10^1	1.57×10^1	0.48	7.11×10^6	0.67
12	3	0.1	100	0.82	0.54	3.67	9.8	9.03×10^4	1.79×10^1	1.56×10^1	0.52	7.12×10^6	0.67
12	3	0.1	1000	0.82	0.54	3.67	9.8	9.04×10^4	1.79×10^1	1.56×10^1	0.54	7.13×10^6	0.67
12	3	0.2	10	0.84	0.57	3.57	10.1	1.24×10^5	1.84×10^1	1.36×10^1	0.69	6.95×10^6	0.67
12	3	0.2	100	0.87	0.60	3.46	10.4	1.78×10^5	2.00×10^1	1.18×10^1	0.67	6.66×10^6	0.70
12	3	0.2	1000	0.89	0.62	3.38	10.6	2.30×10^5	2.14×10^1	1.08×10^1	0.76	6.48×10^6	0.72
12	4	0.1	10	0.86	0.60	4.65	10.3	1.61×10^5	2.56×10^1	2.64×10^1	0.66	1.11×10^7	0.57
12	4	0.1	100	0.86	0.60	4.63	10.4	1.67×10^5	2.56×10^1	2.61×10^1	0.78	1.11×10^7	0.57
12	4	0.1	1000	0.87	0.60	4.61	10.4	1.78×10^5	2.56×10^1	2.62×10^1	0.76	1.11×10^7	0.57
12	4	0.2	10	0.88	0.63	4.53	10.6	2.15×10^5	2.61×10^1	2.39×10^1	0.63	1.09×10^7	0.57
12	4	0.2	100	0.91	0.66	4.38	11.0	3.20×10^5	2.75×10^1	2.14×10^1	0.65	1.06×10^7	0.62
12	4	0.2	1000	1.13	0.93	3.53	13.6	5.50×10^6	1.33×10^2	1.59×10^{-4}	0.00	7.12×10^6	0.61
12	4	0.3	10	0.93	0.67	4.31	11.1	3.96×10^5	2.72×10^1	2.17×10^1	0.56	1.05×10^7	0.66
14	2	0.1	10	0.86	0.55	2.34	12.0	1.13×10^5	9.86×10^0	3.49×10^0	0.35	2.23×10^6	0.90
14	2	0.1	100	0.86	0.55	2.34	12.0	1.13×10^5	9.85×10^0	3.49×10^0	0.36	2.23×10^6	0.90
14	2	0.1	1000	0.86	0.55	2.34	12.0	1.13×10^5	9.85×10^0	3.49×10^0	0.36	2.23×10^6	0.90
14	2	0.2	10	0.91	0.59	2.21	12.7	2.42×10^5	1.25×10^1	2.32×10^0	0.57	1.73×10^6	0.93
14	2	0.2	100	0.89	0.62	2.24	12.5	2.02×10^5	1.20×10^1	1.17×10^{-3}	0.00	1.36×10^6	0.85
14	2	0.3	10	0.90	0.62	2.22	12.6	2.26×10^5	1.24×10^1	7.89×10^{-3}	0.00	1.28×10^6	0.84
14	3	0.1	10	0.89	0.60	3.36	12.5	2.03×10^5	1.79×10^1	1.21×10^1	0.51	6.46×10^6	0.71
14	3	0.1	100	0.89	0.60	3.35	12.5	2.04×10^5	1.79×10^1	1.21×10^1	0.54	6.46×10^6	0.71
14	3	0.1	1000	0.89	0.60	3.35	12.5	2.05×10^5	1.80×10^1	1.20×10^1	0.53	6.47×10^6	0.71
14	3	0.2	10	0.91	0.62	3.28	12.8	2.72×10^5	1.91×10^1	1.07×10^1	0.61	6.29×10^6	0.70
14	3	0.3	100	1.08	0.84	2.79	15.1	3.13×10^6	7.22×10^1	3.55×10^{-4}	0.00	3.59×10^6	0.70
14	4	0.1	10	0.94	0.65	4.27	13.1	3.91×10^5	2.49×10^1	2.17×10^1	0.63	1.05×10^7	0.60
14	4	0.1	100	0.94	0.65	4.26	13.2	4.05×10^5	2.49×10^1	2.29×10^1	0.48	1.05×10^7	0.60
14	4	0.1	1000	0.98	0.67	4.10	13.7	6.98×10^5	3.11×10^1	2.52×10^1	0.58	1.02×10^7	0.61
14	4	0.2	10	0.95	0.67	4.20	13.3	4.90×10^5	2.55×10^1	2.02×10^1	0.66	1.04×10^7	0.59
14	4	0.2	100	1.04	0.74	3.86	14.5	1.74×10^6	4.71×10^1	2.13×10^1	0.78	9.60×10^6	0.58
14	4	0.2	1000	1.11	0.79	3.59	15.6	5.46×10^6	8.42×10^1	3.14×10^1	0.84	9.15×10^6	0.58

[51] **Acknowledgments.** This work was sponsored by the U.S. National Science Foundation under grant EAR-0449517 and Microsoft A. Richard Newton Breakthrough Research Award. The author thanks the Associate Editor and two anonymous referees for careful reviews.

References

Abbott, D., L. Burgess, J. Longhi, and W. H. F. Smith (1994), An empirical thermal history of the Earth's upper mantle, *J. Geophys. Res.*, *99*, 13,835–13,850.

Bercovici, D. (2003), The generation of plate tectonics from mantle convection, *Earth Planet. Sci. Lett.*, *205*, 107–121.

Bercovici, D., and S. Karato (2003), Theoretical analysis of shear localization in the lithosphere, *Rev. Mineral. Geochem.*, *51*, 387–421.

Bercovici, D., G. Schubert, and G. A. Glatzmaier (1992), Three-dimensional, infinite Prandtl number, compressible convection in a basally heated spherical shell, *J. Fluid Mech.*, *239*, 683–719.

Bercovici, D., Y. Ricard, and M. A. Richards (2000), The relation between mantle dynamics and plate tectonics: A primer, in *The History and Dynamics of Global Plate Motions*, edited by M. A. Richards, R. G. Gordon, and R. D. van der Hilst, pp. 5–46, AGU, Washington, D. C.

Bleeker, W. (2003), The late Archean record: A puzzle in ca. 35 pieces, *Lithos*, *71*, 99–134.

Bradley, D. C. (2008), Passive margins through Earth history, *Earth Sci. Rev.*, *91*, 1–26.

Busse, F. H. (1967), On the stability of two-dimensional convection in a layer heated from below, *Z. Angew. Math. Phys.*, *46*, 140–150.

Byerlee, J. (1978), Friction of rocks, *Pure Appl. Geophys.*, *116*, 615–626.

Christensen, U. (1984), Convection with pressure- and temperature-dependent non-Newtonian rheology, *Geophys. J. R. Astron. Soc.*, *77*, 343–384.

Christensen, U. R. (1985), Thermal evolution models for the Earth, *J. Geophys. Res.*, *90*, 2995–3007.

Christensen, U. R., and D. A. Yuen (1984), The interaction of a subducting lithospheric slab with a chemical or phase boundary, *J. Geophys. Res.*, *89*, 4389–4402.

Condie, K. C., and V. Pease (Eds.) (2008), *When Did Plate Tectonics Begin on Planet Earth?*, Geol. Soc. of Am., Boulder, Colo.

Conrad, C. P., and B. H. Hager (1999), Effects of plate bending and fault strength at subduction zones on plate dynamics, *J. Geophys. Res.*, *104*, 17,551–17,571.

Crisp, J. A. (1984), Rates of magma emplacement and volcanic output, *J. Volcanol. Geotherm. Res.*, *20*, 177–211.

Daly, S. F. (1980), Convection with decaying heat sources: Constant viscosity, *Geophys. J. R. Astron. Soc.*, *61*, 519–547.

Davies, G. F. (2009), Effect of plate bending on the Urey ratio and the thermal evolution of the mantle, *Earth Planet. Sci. Lett.*, *287*, 513–518.

Deschamps, F., P. J. Tackley, and T. Nakagawa (2010), Temperature and heat flux scalings for isoviscous thermal convection in spherical geometry, *Geophys. J. Int.*, *182*, 137–154.

Evans, R. L., G. Hirth, K. Baba, D. Forsyth, A. Chave, and R. Mackie (2005), Geophysical evidence from the MELT area for compositional controls on oceanic plates, *Nature*, *437*, 249–252.

Faul, U. H., and I. Jackson (2007), Diffusion creep of dry, melt-free olivine, *J. Geophys. Res.*, *112*, B04204, doi:10.1029/2006JB004586.

Fei, Y., J. Van Orman, J. Li, W. van Westrennen, C. Sanloup, W. Minarik, K. Hirose, T. Komabayashi, M. Walter, and K. Funakoshi (2004), Experimentally determined postspinel transformation boundary in Mg_2SiO_4 using MgO as an internal pressure standard and its geophysical implications, *J. Geophys. Res.*, *109*, B02305, doi:10.1029/2003JB002652.

Foley, B. J., and T. W. Becker (2009), Generation of plate-like behavior and mantle heterogeneity from a spherical, viscoplastic convection model, *Geochem. Geophys. Geosyst.*, *10*, Q08001, doi:10.1029/2009GC002378.

Gordon, R. G., and S. Stein (1992), Global tectonics and space geodesy, *Science*, *256*, 333–342.

Gurnis, M., S. Zhong, and J. Toth (2000), On the competing roles of fault reactivation and brittle failure in generating plate tectonics from mantle convection, in *The History and Dynamics of Global Plate Motions*, edited by M. A. Richards, R. G. Gordon, and R. D. van der Hilst, pp. 73–94, AGU, Washington, D. C.

Gurnis, M., C. Hall, and L. Lavier (2004), Evolving force balance during incipient subduction, *Geochem. Geophys. Geosyst.*, *5*, Q07001, doi:10.1029/2003GC000681.

Hager, B. H. (1984), Subducted slabs and the geoid: Constraints on mantle rheology and flow, *J. Geophys. Res.*, *89*, 6003–6015.

Hager, B. H. (1991), Mantle viscosity: A comparison of models from postglacial rebound and from the geoid, plate driving forces, and advected heat flux, in *Glacial Isostasy, Sea-Level and Mantle Rheology*, edited by R. Sabadini, K. Lambeck, and E. Boschi, pp. 493–513, Kluwer Acad., Dordrecht, Netherlands.

Harrison, T. M. (2009), The Hadean crust: Evidence from >4 Ga zircon, *Annu. Rev. Earth Planet. Sci.*, *37*, 479–505.

Harrison, T. M., J. Blichert-Toft, W. Müller, F. Albarede, P. Holden, and S. J. Mojzsis (2005), Heterogeneous Hadean hafnium: Evidence of continental crust at 4.4 to 4.5 Ga, *Science*, *310*, 1947–1950.

Herzberg, C., P. D. Asimow, N. Arndt, Y. Niu, C. M. Lesher, J. G. Fitton, M. J. Cheadle, and A. D. Saunders (2007), Temperatures in ambient mantle and plumes: Constraints from basalts, picrites, and komatiites, *Geochem. Geophys. Geosyst.*, *8*, Q02206, doi:10.1029/2006GC001390.

Herzberg, C., K. Condie, and J. Korenaga (2010), Thermal evolution of the Earth and its petrological expression, *Earth Planet. Sci. Lett.*, *292*, 79–88.

Hirth, G., and D. L. Kohlstedt (1996), Water in the oceanic mantle: Implications for rheology, melt extraction, and the evolution of the lithosphere, *Earth Planet. Sci. Lett.*, *144*, 93–108.

Howard, L. N. (1966), Convection at high Rayleigh number, in *Proceedings of the Eleventh International Congress of Applied Mechanics*, edited by H. Gortler, pp. 1109–1115, Springer, New York.

Jarvis, G. T., and D. P. McKenzie (1980), Convection in a compressible fluid with infinite Prandtl number, *J. Fluid Mech.*, *96*, 515–583.

Karato, S. (2008), *Deformation of Earth Materials: Introduction to the Rheology of the Solid Earth*, Cambridge Univ. Press, Cambridge, U. K.

Karato, S., and P. Wu (1993), Rheology of the upper mantle: A synthesis, *Science*, *260*, 771–778.

Karato, S., M. S. Paterson, and J. D. Fitzgerald (1986), Rheology of synthetic olivine aggregates: Influence of grain size and water, *J. Geophys. Res.*, *91*, 8151–8176.

Katsura, T., et al. (2003), Post-spinel transition in Mg_2SiO_4 determined by high *P-T* in situ X-ray deffractometry, *Phys. Earth Planet. Inter.*, *136*, 11–24.

Kido, M., and O. Cadek (1997), Inferences of viscosity from the oceanic geoid: Indication of a low viscosity zone below the 660-km discontinuity, *Earth Planet. Sci. Lett.*, *151*, 125–137.

King, S. D. (1995), Models of mantle viscosity, in *Global Earth Physics: A Handbook of Physical Constants*, pp. 227–236, AGU, Washington, D. C.

Korenaga, J. (2003), Energetics of mantle convection and the fate of fossil heat, *Geophys. Res. Lett.*, *30*(8), 1437, doi:10.1029/2003GL016982.

Korenaga, J. (2006), Archean geodynamics and the thermal evolution of Earth, in *Archean Geodynamics and Environments*, edited by K. Benn, J.-C. Mareschal, and K. Condie, pp. 7–32, AGU, Washington, D. C.

Korenaga, J. (2007), Thermal cracking and the deep hydration of oceanic lithosphere: A key to the generation of plate tectonics?, *J. Geophys. Res.*, *112*, B05408, doi:10.1029/2006JB004502.

Korenaga, J. (2008a), Urey ratio and the structure and evolution of Earth's mantle, *Rev. Geophys.*, *46*, RG2007, doi:10.1029/2007RG000241.

Korenaga, J. (2008b), Plate tectonics, flood basalts, and the evolution of Earth's oceans, *Terra Nova*, *20*, 419–439.

Korenaga, J. (2009), Scaling of stagnant-lid convection with Arrhenius rheology and the effects of mantle melting, *Geophys. J. Int.*, *179*, 154–170.

Korenaga, J., and T. H. Jordan (2003), Physics of multiscale convection in Earth's mantle: Onset of sublithospheric convection, *J. Geophys. Res.*, *108*(B7), 2333, doi:10.1029/2002JB001760.

Korenaga, J., and S. Karato (2008), A new analysis of experimental data on olivine rheology, *J. Geophys. Res.*, *113*, B02403, doi:10.1029/2007JB005100.

Korenaga, J., P. B. Kelemen, and W. S. Holbrook (2002), Methods for resolving the origin of large igneous provinces from crustal seismology, *J. Geophys. Res.*, *107*(B9), 2178, doi:10.1029/2001JB001030.

Landuyt, W., and D. Bercovici (2009), Variations in planetary convection via the effect of climate on damage, *Earth Planet. Sci. Lett.*, *277*, 29–37.

Landuyt, W., D. Bercovici, and Y. Ricard (2008), Plate generation and two-phase damage theory in a model of mantle convection, *Geophys. J. Int.*, *174*, 1065–1080.

Lenardic, A., F. Nimmo, and L. Moresi (2004), Growth of the hemispheric dichotomy and the cessation of plate tectonics on Mars, *J. Geophys. Res.*, *109*, E02003, doi:10.1029/2003JE002172.

McKenzie, D. P., J. M. Roberts, and N. O. Weiss (1974), Convection in the Earth's mantle: Towards a numerical simulation, *J. Fluid Mech.*, *62*, 465–538.

Mei, S., and D. L. Kohlstedt (2000a), Influence of water on plastic deformation of olivine aggregates: 1. Diffusion creep regime, *J. Geophys. Res.*, *105*, 21,457–21,469.

Mei, S., and D. L. Kohlstedt (2000b), Influence of water on plastic deformation of olivine aggregates: 2. Dislocation creep regime, *J. Geophys. Res.*, *105*, 21,471–21,481.

Mojzsis, S. J., T. M. Harrison, and R. T. Pidgeon (2001), Oxygen-isotope evidence from ancient zircons for liquid water at the Earth's surface 4,300 Myr ago, *Nature*, *409*, 178–181.

Moresi, L., and V. Solomatov (1998), Mantle convection with a brittle lithosphere: Thoughts on the global tectonic styles of the Earth and Venus, *Geophys. J. Int.*, *133*, 669–682.

Ogawa, M. (2003), Plate-like regime of a numerically modeled thermal convection in a fluid with temperature-, pressure-, and stress-history-dependent viscosity, *J. Geophys. Res.*, *108*(B2), 2067, doi:10.1029/2000JB000069.

O'Neill, C., and A. Lenardic (2007), Geological consequences of super-sized Earths, *Geophys. Res. Lett.*, *34*, L19204, doi:10.1029/2007GL030598.

O'Neill, C., A. Lenardic, L. Moresi, T. H. Torsvik, and C.-T. Lee (2007), Episodic Precambrian subduction, *Earth Planet. Sci. Lett.*, *262*, 552–562.

Oxburgh, E. R., and E. M. Parmentier (1977), Compositional and density stratification in oceanic lithosphere—Causes and consequences, *J. Geol. Soc. London*, *133*, 343–355.

Richards, M. A., W.-S. Yang, J. R. Baumgardner, and H.-P. Bunge (2001), Role of a low-viscosity zone in stabilizing plate tectonics: Implications for comparative terrestrial planetology, *Geochem. Geophys. Geosyst.*, *2*(8), doi:10.1029/2000GC000115.

Ringwood, A. E., and T. Irifune (1988), Nature of the 650-km seismic discontinuity—Implications for mantle dynamics and differentiation, *Nature*, *331*, 131–136.

Schubert, G., D. L. Turcotte, and P. Olson (2001), *Mantle Convection in the Earth and Planets*, Cambridge Univ. Press, Cambridge, U. K.

Soldati, G., L. Boschi, F. Deschamps, and D. Giardini (2009), Inferring radial models of mantle viscosity from gravity (GRACE) data and an evolutionary algorithm, *Phys. Earth Planet. Inter.*, *176*, 19–32.

Solheim, L. P., and W. R. Peltier (1994), Avalanche effects in phase transition modulated thermal convection, *J. Geophys. Res.*, *99*, 6997–7018.

Solomatov, V. S. (1996), Can hotter mantle have a larger viscosity?, *Geophys. Res. Lett.*, *23*, 937–940.

Solomatov, V. S. (2004), Initiation of subduction by small-scale convection, *J. Geophys. Res.*, *109*, B01412, doi:10.1029/2003JB002628.

Solomatov, V. S., and L.-N. Moresi (2000), Scaling of time-dependent stagnant lid convection: Application to small-scale convection on Earth and other terrestrial planets, *J. Geophys. Res.*, *105*, 21,795–21,817.

Stein, C., J. Schmalzl, and U. Hansen (2004), The effect of rheological parameters on plate behavior in a self-consistent model of mantle convection, *Phys. Earth Planet. Inter.*, *142*, 225–255.

Stern, R. J. (2005), Evidence from ophiolites, blueschists, and ultrahigh-pressure metamorphic terranes that the modern episode of subduction tectonics began in Neoproterozoic time, *Geology*, *33*, 557–560.

Tackley, P. J. (2000), Self-consistent generation of tectonic plates in time-dependent, three-dimensional mantle convection simulations: 2. Strain

weakening and asthenosphere, *Geochem. Geophys. Geosyst.*, *1*(8), doi:10.1029/2000GC000043.
Tackley, P. J., D. J. Stevenson, G. A. Glatzmaier, and G. Schubert (1993), Effects of an endothermic phase transition at 670 km depth in a spherical model of convection in the Earth's mantle, *Nature*, *361*, 699–704.
van Heck, H. J., and P. J. Tackley (2008), Planforms of self-consistently generated plates in 3D spherical geometry, *Geophys. Res. Lett.*, *35*, L19312, doi:10.1029/2008GL035190.
Van Kranendonk, M. J., R. H. Smithies, A. H. Hickman, and D. Champion (2007), Review: Secular tectonic evolution of Archean continental crust: Interplay between horizontal and vertical processes in the formation of the Pilbara Craton, Australia, *Terra Nova*, *19*, 1–38.
Weinstein, S. A., and P. L. Olson (1992), Thermal convection with non-Newtonian plates, *Geophys. J. Int.*, *111*, 515–530.
Yuen, D. A., D. M. Reuteler, S. Balachandar, V. Steinbach, A. V. Malevsky, and J. J. Smedsmo (1994), Various influences on three-dimensional mantle convection with phase transitions, *Phys. Earth Planet. Inter.*, *86*, 185–203.
Zhong, S., and M. Gurnis (1994), Role of plates and temperature-dependent viscosity in phase change dynamics, *J. Geophys. Res.*, *99*, 15,903–15,917.

J. Korenaga, Department of Geology and Geophysics, Yale University, PO Box 208109, New Haven, CT 06520-8109, USA. (jun.korenaga@yale.edu)